Chapter 2

Geology and thermochronology of Tertiary Cordilleran-style metamorphic core complexes in the Saghand region of central Iran

Geological Society of America Bulletin, 2007, v. 119, p. 961-977.

Charles Verdel[1], Brian P. Wernicke[1], Jahandar Ramezani[2], Jamshid Hassanzadeh[3], Paul R. Renne[4], and Terry L. Spell[5]

(1) Division of Geological and Planetary Sciences, California Institute of Technology, Pasadena, CA 91125

(2) Department of Earth, Atmospheric and Planetary Sciences, Massachusetts Institute of Technology, Cambridge, MA 02139

(3) Department of Geology, University of Tehran, Tehran, Iran

(4) Berkeley Geochronology Center, 2455 Ridge Rd., Berkeley, CA 94709 *and* Department of Earth and Planetary Science, University of California, Berkeley, CA 94720

(5) Department of Geoscience, University of Nevada, Las Vegas, Las Vegas, NV 89154

ABSTRACT

An ~100 km long N-S belt of metamorphic core complexes is localized along the boundary between the Yazd and Tabas tectonic blocks of the central Iranian microcontinent, between the towns of Saghand and Posht-e-Badam. Amphibolite facies mylonitic gneisses are structurally overlain by east-tilted supracrustral rocks including thick (>1 km), steeply dipping, nonmarine siliciclastic and volcanic strata. Near the detachment (the Neybaz-Chatak fault), the gneisses are generally overprinted by chlorite brecciation. Cross-cutting relationships along with U-Pb zircon and $^{40}Ar/^{39}Ar$ age data indicate that migmatization, mylonitic deformation, volcanism and sedimentation all occurred in the middle Eocene, between ~49 and 41 Ma. The westernmost portion of the Tabas block immediately east of the complexes is an east-tilted crustal section of Neoproterozoic/Cambrian crystalline rocks and metasedimentary strata >10 km thick. $^{40}Ar/^{39}Ar$ biotite ages of 150-160 Ma from structurally deep parts of the section contrast with ages of 218-295 Ma from shallower parts and suggest Late Jurassic tilting of the crustal section. These results define three events: (1) a Late Jurassic period of upper crustal cooling of the western Tabas block, which corresponds to regional Jura-Cretaceous tectonism and erosion recorded by a strong angular unconformity below mid-Cretaceous strata throughout central Iran; (2) profound ~EW middle Eocene crustal extension, plutonism and volcanism (ca. 44-40 Ma); and (3) ~2-3 km of early Miocene (ca. 20 Ma) erosional exhumation of both core complex and Tabas block assemblages at uppermost crustal levels, resulting from significant north-south shortening. The discovery of these and other complexes within the mid-Tertiary magmatic arcs of Iran demonstrates that Cordilleran-style core-complexes are an important tectonic element in all major segments of the Alpine-Himalayan orogenic system.

INTRODUCTION

The Cenozoic geology of Iran has traditionally been viewed in terms of two dominant events: widespread and voluminous Eocene to Oligocene primarily arc-related volcanism (e.g., Forster et al., 1972) (Figure 1) and accompanying rapid sedimentation, and Miocene and younger folding, thrusting and strike-slip faulting accommodating the collision between Arabia and Eurasia (e.g., Stöcklin, 1968). More recently, some authors have proposed an Eocene to Miocene phase of crustal extension in Iran and adjacent regions to explain the local alkaline affinity of Tertiary volcanism and the onset of rapid sedimentation (Hassanzadeh et al., 2002; Vincent et al., 2005). Recognition of tectonic elements of Late Cretaceous and younger age associated with significant crustal extension in Iran has included reports of domino-style normal faulting in the Golpaygan region (Tillman et al., 1981) and rapid exhumation of mylonitic crystalline rocks along extensional detachment faults in the Takab, Biarjmand and Posht-e-Badam areas (Stockli et al., 2004; Hassanzadeh et al., 2005; Kargaran et al., 2006, respectively; Figure 1).

In this paper we present the results of field and analytical work in the Saghand and Posht-e-Badam area of central Iran, where we have documented a north-trending belt of domiform mountain ranges exhibiting the traits of the mid-Tertiary metamorphic core complexes in the Sonora Desert region of southwestern North America (e.g., Davis, 1980; Reynolds, 1985). These include mylonitized, high-grade granitic rocks lying below a low-angle detachment fault, with associated chlorite brecciation; low-grade to unmetamorphosed upper plate rocks; and a supradetachment basin containing a thick succession of scarp-facies nonmarine strata. We first describe the regional and local geological setting of these central Iranian ranges based on previous work, and then systematically describe the extensional tectonic elements. Building on an extensive database of U-Pb geochronology of crystalline and volcanic rocks (Ramezani and Tucker, 2003) we then present new U-Pb, (U-Th)/He and $^{40}Ar/^{39}Ar$ data that refine the timing of extensional deformation as well as earlier and later periods of major deformation, and discuss the significance of this data for the Tertiary evolution of the Tethysides.

TECTONIC SETTING

The Iranian segment of the Alpine-Himalayan orogenic system has a complex Permian through Quaternary history of successive rifting and collision, but nonetheless most of Iran is underlain by a relatively concordant blanket of Paleozoic platform sediments similar to those on the Arabian platform (e.g., Stöcklin, 1968). It is therefore generally believed that the major continental blocks in Iran, as outlined by narrow belts of Mesozoic ophiolitic rocks, had a common origin in a cratonic platform along the northern flank of Gondwana in late Paleozoic time (e.g., Ramezani and Tucker, 2003). Permian through Quaternary reconstructions of the Tethysides in the Middle East accordingly involve progressive break up and transfer of fragments of northern Gondwana and their accretion to the southern flank of Eurasia (e.g., Sengör and Natal'in, 1996). The most recent event of this type is the mid-Tertiary rifting of Arabia away from Africa and its Miocene collision with Asia by closure of the Neotethys oceanic tract (e.g., Axen et al., 2001; McQuarrie et al., 2003), ultimately forming the folded belts of the Zagros Mountains to the south and the Alborz-Kopet Dagh ranges to the north (Figure 1). The collisional suture between Arabia and Eurasia lies along or perhaps somewhat north of the Zagros thrust zone, which juxtaposes folded and thrusted strata of the Arabian platform against a stratigraphically and structurally more complex, marginal assemblage referred to as the Sanandaj-Sirjan zone (Figure 1).

Prior to the collision, plate convergence involved northward subduction of ~1300 km of Neotethyan oceanic lithosphere (e.g., McQuarrie et al., 2003), resulting in Andean-type magmatic arcs on the overriding continental plates that reach from the Balkan Peninsula to Afghanistan. The bulk of the Paleogene magmatic rocks in Iran are traditionally grouped into three belts: Alborz in the north, Urumieh-Dokhtar across central Iran, and Lut in the east (Figure 1). Between the Alborz and Urumieh-Dokhtar belts lies a large region of relatively low topography that includes the Central-East Iranian Microcontinent (CEIM), as outlined by major faults (Takin, 1972).

The Saghand area lies in the western portion of the CEIM, about 100 km north-northeast of the axis of the Urumieh-Dokhtar arc (Figure 1). The CEIM is subdivided into three fault-bounded blocks, including (from east to west) the Lut, Tabas and Yazd blocks (Figure 1; e.g., Alavi, 1991). The boundary zone between the Tabas and Yazd blocks, the Kashmar-Kerman tectonic zone of Ramezani and Tucker (2003), forms a 50-100 km-wide, 600 km-long concave-east belt (Figure 1) that exposes stratigraphically and structurally deep crustal levels (Cambrian stratified rocks, various crystalline units) that contrast with predominantly unmetamorphosed Mesozoic and younger rocks exposed elsewhere in the two blocks.

GEOLOGY OF THE SAGHAND REGION

Previous investigations in the Saghand area have included systematic mapping at scales of 1:100,000 to 1:500,000 (Valeh and Haghipour, 1970; Haghipour, 1977a and b; Haghipour et al., 1977), and the detailed U-Pb zircon study of magmatic rocks in the area (Ramezani and Tucker, 2003). The area is crossed by two strike-slip faults of unknown age and net slip, the Posht-e-Badam and Chapedony faults (Figure 2). Ramezani and Tucker (2003) subdivided the area into three lithotectonic domains, including an eastern, a central and a western domain, based on lithostratigraphic and age characteristics. The eastern and central domains are juxtaposed along the Posht-e-Badam fault. The central domain is faulted over the western domain along the Neybaz and Chatak faults, which dip shallowly to moderately east or northeast, and are not overlapped by any pre-Neogene strata. Although the contact between central and western domains is mainly exposed in two semi-continuous bands, it appears that a single low-angle fault system (the Neybaz-Chatak fault) juxtaposes the two domains over an along-strike distance of about 90 km (Figure 2).

Bedrock exposures in the central and eastern domains constitute 1) stratified rocks that range in age from Ediacaran/Cambrian to Neogene (Figure 2, upper left legend); 2) crystalline metamorphic complexes that include steeply foliated medium-grade felsic gneisses, schists, amphibolites and marble known as the Boneh-Shurow (eastern domain) and Posht-e-Badam (central domain) complexes, and 3) magmatic intrusive and sub-extrusive rocks of Early Cambrian (eastern domain) and Late Triassic (central domain) age (Figure 2, lower right legend). The western domain is dominated by Eocene deep-seated metamorphic rocks and magmatic intrusions (Figure 2, see also units defined in the lower right legend). The rock units relevant to this study are described in more detail below. Stated age data in this section are those of Ramezani and Tucker (2003).

Stratified rocks

The oldest stratified rocks include a thick succession of Ediacaran to early Cambrian weakly metamorphosed graywackes, volcaniclastic rocks and basaltic lavas, collectively referred to as the Tashk Formation. It contains detrital zircons as young as 627 Ma and was intruded by 533 Ma granitoid plutons. The Tashk Formation is overlain by the Cambrian Volcano-Sedimentary Unit (CVSU) of Ramezani and Tucker (2003). These units are overlain in angular unconformity by Permian and Triassic shallow marine carbonates.

Terrigenous and carbonaceous rocks of mid-Cretaceous age containing Aptian to Cenomanian fossils (e.g., *Orbitolina*) lie in angular unconformity on older units ranging in age from Cambrian through Triassic (Haghipour et al., 1977). Although the pre-Cretaceous hiatus spans between ca. 100 to 400 My within the Kashmar-Kerman tectonic zone, in the interior of the Yazd and Tabas blocks strongly folded marine strata as young as Middle Jurassic rest in angular unconformity beneath the mid-Cretaceous strata (Haghipour et al., 1977). The stratigraphic record thus indicates that significant crustal shortening occurred within the central Iranian structural blocks between mid-Jurassic and mid-Cretaceous time and was concomitant with substantial erosion, particularly within the Kashmar-Kerman tectonic zone.

Volcanic rocks and associated sedimentary strata of Eocene age are widespread within the CEIM and throughout Iran (Figure 1), but are restricted to two relatively small areas in the Saghand region (Haghipour et al., 1977), one along the northwest flank of Kalut-e-Chapedony and another along the northeast side of Khoshoumi Mountain (Figure 2). In the latter location, Haghipour et al. (1977) reported nummulitic marls indicating marine deposition, at least in part. As elaborated below, our observations of a steeply dipping section of these strata in excess of 1000 meters thick suggest primarily non-marine deposition in a rapidly subsiding basin, but confirm the Eocene age assignment of Haghipour et al. (1977).

The Eocene strata are overlain in angular unconformity by poorly consolidated evaporitic sandstones and mudstones which are probably Miocene or Pliocene in age (Haghipour et al., 1977). Near Saghand, these strata are at least several hundred meters thick and display a complex pattern of faulting and folding that suggests significant contractile deformation.

Crystalline rocks

Within each of the five ranges that comprise the eastern domain, the first-order structural pattern is that of an east-tilted crustal section, with Cretaceous strata exposed in the eastern portions of the ranges, east-dipping stratified rocks of the Tashk Formation and CVSU occupying the central portions, and deep-seated crystalline rocks of the Boneh-Shurow complex cropping out in the west (Figure 2). The primary contact between the stratified rocks and subjacent crystalline rocks in both the central and eastern domains is a moderately to steeply east-dipping ductile shear zone. Plutonism and metamophism in the Boneh-Shurow complex occurred at ~545 Ma. Emplacement of granitoid plutons and intermediate to felsic volcanism associated with the CVSU occurred over a narrow temporal window of 533 to 525 Ma.

The western domain is composed almost entirely of high-grade gneissic rocks comprising the Chapedony complex. This complex was long considered the oldest of the Precambrian units in the Saghand region based on its high metamorphic grade (Stöcklin, 1968; Haghipour et al., 1977), but U-Pb zircon dating demonstrates a middle Eocene intrusive age for the oldest components of these gneisses. Zircons from both syn-kinematic gneiss and migmatitic leucosomes derived from them have previously yielded concordia lower intercept ages of ca. 46 Ma (Ramezani and Tucker, 2003). The majority of the Chapedony complex is comprised of gneiss, with lesser amounts of migmatite, anatectite, schist, marble and calc-silicate rock. The gneisses are locally amphibolitic but are predominantly medium to coarse biotite-kspar-plagioclase-quartz gneiss with rare clinopyroxene and garnet. Medium to high metamorphic grade is indicated by large areas of migmatite and anatectite within the complex (Ramezani and Tucker, 2003).

Two post-metamorphic intrusions crop out at Daranjir Mountain (Figure 2). The Daranjir diorite (U-Pb age 43.4 +/- 0.2 Ma) is apparently the older of the intrusions. The Khoshoumi granite (U-Pb age 44.3 +/- 1.1 Ma) overlaps in age, but intrudes both the Daranjir diorite and gneisses of the Chapedony complex. These ages and cross-cutting relationships thus constrain metamorphism of the Chapedony complex to have occurred between 49 and 44 Ma (Ramezani and Tucker, 2003).

STRUCTURAL AND STRATIGRAPHIC OBSERVATIONS OF THE NEYBAZ-CHATAK DETACHMENT SYSTEM

Our new field observations include 1) geological mapping of a ~6 km-long transect across the detachment system along the northeast flank of Khoshoumi Mountain (western domain), where all of the primary extensional tectonic elements are exposed; 2) mesoscopic structural data from mylonitic gneisses at Khoshoumi Mountain, Neybaz Mountain and Kalut-e-Chapedony; 3) structural microanalysis of lower plate mylonitic gneisses; 4) photo-documentation of key structural and stratigraphic relationships in the area; and 5) structural reconnaissance of the western end of Boneh-Shurow Mountain using high-resolution satellite imagery.

Neybaz-Chatak detachment fault and hanging wall splays

The Neybaz-Chatak detachment system without exception emplaces lower temperature rock assemblages on top of higher. On the east side of Khoushoumi Mountain, the detachment emplaces Eocene supradetachemnt basin deposits and weakly metamorphosed to unmetamorphosed CVSU over mylonitic gneiss of the Chapedony complex (Figure 2). At Neybaz Mountain and Kalut-e-Chatak it emplaces medium-grade greenstones of the Posht-e-Badam complex over high-grade gneiss, and at the southeast tip of Kalut-e-Chapedony it emplaces unmetamorphosed Cretaceous limestone over high-grade gneiss. Above the main contact with Chapedony complex gneisses along the eastern flanks of Neybaz Mountain and Khoshoumi Mountain, low- and high-angle splays juxtapose lower grade rocks on higher, or where both units are stratified, younger rocks on top of older.

Along the Khoshoumi Mountain transect, the detachment juxtaposes strongly gouged and brecciated CVSU over mylonitic gneiss, and a hanging wall normal fault juxtaposes Eocene sedimentary rocks against CVSU (Figure 3). The detachment contact in general dips gently to the north, but is strongly curviplanar, forming an E- to NE-trending antiform-synform pair (Figures 3 and 4a). In outcrop, the detachment varies from being a diffuse zone of gouge and breccia a few meters wide to a sharply defined plane (Figure 5a). The gouge zones associated with the detachment and its hanging wall splays are at least tens of meters thick (Figure 5b) and exhibit phacoidal structure, with lozenge-shaped blocks of ~1 to 10 m in maximum dimension set in a matrix of gouge (Figure 5c).

Immediately below exposures of the detachment, tabular zones of chlorite breccia were observed at Khoshoumi Mountain (Figure 5a), Neybaz Mountain (Figure 6a) and along the western flank of Kalut-e-Chapedony. At the latter locality the detachment emplaces Cretaceous limestone on chlorite breccia of mylonitic gneiss, with brecciation affecting a structural thickness of mylonite (measured perpendicular to foliation) of about 100 m. Brecciation and chloritization become much less intense downward through the zone, which has a well defined base (Figure 5d).

Mylonites

As first observed by Haghipour et al. (1977), "huge parts" of the Chapedony complex are mylonitic. Mylonitization of augen gneiss and late-stage pegmatites within the gneiss is widespread on Khoshoumi Mountain, Neybaz Mountain (Figures 6b and 6c) and at Kalut-e-Chapedony (Figure 5e). The mylonites typically are composed of feldspar porphyroclasts in a matrix of biotite and fine-grained, recrystallized quartz and feldspar (Figure 6d). Recrystallized quartz and feldspar grains average ~100 µm and ~25 µm in diameter, respectively. Quartz is typically recrystallized by subgrain rotation, while recrystallization of feldspar is primarily from "bulging" recrystallization (e.g., Passchier and Trouw, 2005). These textures, along with abundant myrmekite, suggest that mylonitization occurred in the upper part of the medium-grade conditions field (450-600° C) of Passchier and Trouw (2005). Textures range from protomylonite to ultramylonite, often within single outcrops (Figure 6b). Although lineation or foliation may be difficult to detect in some outcrops, the mylonites tend to be well developed L-S tectonites with low to moderate dip and plunge, with the lineation bisecting conjugate joints (Figure 5e).

Foliation and lineation orientations were measured in three areas: on the south side of Neybaz Mountain, in the mapped transect on the east side of Khoshoumi Mountain (Figure 3), and in the central part of Kalut-e-Chapedony (Figure 2). In the latter two areas, measurements were distributed over an area of 1-2 km^2. The orientations at Kalut-e-Chapedony are distinctly different from those in the two areas to the south. At Kalut-e-Chapedony, foliation typically strikes roughly north-south and dips fairly gently to the west, with lineation plunging an average of 12°WSW (Figure 7a). At Neybaz and

Khoshoumi Mountains, attitudes are more scattered, but, on average, foliation dips north and lineation plunges 43°N (Figure 7b).

Well developed S-C texture is preserved in mylonitic orthogneiss along the southern flank of Neybaz Mountain, yielding top-to-the-north sense of shear (Figure 6c). Oriented samples of eight other mylonites, five from Kalut-e-Chapedony and three from Khoshoumi Mountain, were slabbed and sectioned parallel to lineation and perpendicular to foliation to evaluate sense of shear. The Kalut-e-Chapedony samples yielded three top-to-the-west determinations and one top-to-the-east (Figure 7a). The samples from Khoshoumi Mountain yielded two top-to-the-south and one top-to-the-north determinations (Figure 7b). The occurrence of oppositely directed shear sense indicators is quite common, if not ubiquitous, in mylonitic rocks (Hippertt and Tohver, 1999) and may suggest an important component of "pure shear" contraction normal to the flow direction (e.g., Lee et al., 1987).

Supradetachment and post-extensional basinal deposits and structures

As mentioned above, at least 1000 m of Tertiary non-marine sandstone, siltstone, conglomerate, breccia and volcanic rocks are exposed on the northeast flank of Khoshoumi Mountain (Figure 4a). In the map transect (Figure 3), these strata dip steeply southeastward, and are truncated along a moderately to steeply north-dipping normal fault which emplaces them on top of brecciated Cambrian strata. Tectonic lenses of Cretaceous conglomerate are locally present along the fault contact. The Tertiary strata are intruded by a dacite plug, which exhibits well developed flow foliation and consists of an older phase to the west (Tev1 on Figure 3) and a younger phase to the east (Tev2 on Figure 3). The intrusive contact is sub-parallel to the flow foliation, and both dip steeply inward toward the dome in a radial pattern. Attitudes of bedding in the country rock appear to be deflected into parallelism with the margins of the plug as a result of emplacement (Figure 3). Small outliers of the main intrusive occur on the southwestern side, one of which intrudes brecciated CVSU strata south of the normal fault that juxtaposes Cambrian and Tertiary rocks. Given the kilometer-scale offset along the normal fault and the lack of brecciation in the outlier within the Cambrian strata, we interpret these relations to indicate that intrusion occurred after faulting and brecciation of the CVSU. The steep inward dips of flow foliation around the dome further suggest that intrusion may also have post-dated most tilting of the Tertiary section, assuming the plug intruded vertically.

The lower part of the Tertiary section southwest of the intrusive plug is primarily sandstone and siltstone but contains at least one rock avalanche deposit a few meters thick containing clasts of Cambrian volcanic rocks (Figure 5f). As developed further after discussion of geochronological data from the area, we interpret these strata as a fault scarp facies developed in the early stages of detachment faulting, whereby the upper crust was fragmented into fault blocks, just prior to major rotation of hanging wall strata and final ascent of mylonitic gneisses to the surface.

Along the northeast margin of Khoshoumi Mountain, a marked angular unconformity is observed between the steeply tilted Tertiary strata and overlying Neogene(?) nonmarine strata, which dip gently northeastward (Figures 3, 4a). The origin of tilting of the younger strata is not clear from relations around Khoshoumi Mountain. However, in the extensive exposures of these deposits in low-relief badlands just east of Saghand (Haghipour et al., 1977), a large, open, gently west-plunging anticline with gently to moderately dipping limbs is developed within these deposits. The anticline is cored by basement rocks of the Boneh Shurow complex, and is aligned with the long axis of the topographic ridge comprising Boneh-Shurow Mountain and Tashk Mountain (Figures 2 and 4b). This relationship indicates that some or all of the topography of the region may be controlled by post-extensional, approximately north-south tectonic shortening.

GEOCHRONOLOGY AND THERMOCHRONOLOGY

U-Pb geochronology

We determined one additional U-Pb zircon age from mylonitic (augen) orthogneiss of the Chapedony complex at Neybaz Mountain (sample 2604, Table S1, Figure 2; Figure 6c). This sample consists of mica-rich bands enveloping K-feldspar and plagioclase porphyroclasts. Six single zircon grains were analyzed for Pb and U by the ID-TIMS method at the Geochronology Laboratory at MIT (Lehrmann et al, 2006; Schoene et al, 2006). The U-Pb isotopic dates and the associated uncertainties are calculated using the error propagation algorithm of Ludwig (1980) and are plotted with 2σ uncertainties on a conventional concordia plot (Figure 8). The final uncertainties reported here incorporate both the internal (analytical) and external (systematic) sources of error. The latter includes the U-Pb tracer calibration error as well as the U decay constant errors of Jaffey et al. (1971). The incorporation of systematic errors in the calculated dates is necessary when results from different laboratories and/or different isotopic systems (*e.g.*, U-Pb versus $^{40}Ar/^{39}Ar$) are compared (e.g., Schoene et al., 2006). Details of the U-Pb procedure are provided in Appendix A and Table S1.

Six U-Pb zircon analyses from sample 2604 produced an array of mutually distinctive $^{206}Pb/^{238}U$ dates ranging from 49.35 Ma to 48.97 Ma (Figure 8). Regression of these data to a straight line yields an upper concordia intercept date of 49.66 ± 0.96 Ma (MSWD = 0.1). Alternatively, the three youngest analyses (z3, z5 and z6) overlap within error and yield a weighted mean $^{206}Pb/^{238}U$ date of 49.01 ± 0.12 Ma. The two calculated dates overlap within uncertainties and represent end-member estimates for the timing of zircon crystallization in the rock. These dates are consistent within uncertainties with a less precise 46.8 ± 2.5 Ma zircon date from a nearby gneiss sample previously determined by Ramezani and Tucker (2003). Similarly, our measured ages can be interpreted as the timing of peak-metamorphic and/or anatectic zircon crystallization in the Chapedony complex.

^{40}Ar/^{39}Ar geochronology

The ages of three samples from the Khoshoumi Mountain map transect were determined by $^{40}Ar/^{39}Ar$ geochronology techniques using a CO_2 laser and automated extraction line at the Berkeley Geochronology Center using the Fish Canyon sanidine (28.02 Ma; Renne et al., 1998) as a neutron flux monitor (Figures 3 and 9, Table S2).

Sample 1604 was collected from a layer of biotite-rich volcanic ash within sediments from the hanging wall of the detachment. Samples 1304 and 1404 were collected from the dacite plug that intrudes the sediments (Figure 3). Biotite from the ash has an $^{40}Ar/^{39}Ar$ inverse isochron age of 41.2 ± 2.4 Ma. Plagioclase from sample 1304 has an inverse isochron age of 42.0 ± 1.8 Ma, which is indistinguishable (within uncertainties) from an alkali feldspar age of 40.5 ± 2.5 Ma from sample 1404. Considering that the ash is near the top of the exposed section and assuming the dacite plug postdates both faulting and tilting as discussed in the previous section, these ages suggest that faulting and tilting occurred between 39 and 43 Ma.

In addition, $^{40}Ar/^{39}Ar$ biotite ages were determined for six samples from a transect along Boneh-Shurow and Tashk Mountains (Figure 2, Table S3). These ages represent the time since the samples cooled below the Ar closure temperature in biotite, which is ~300-350°C under conditions of rapid cooling (≥10°C/My) (Harrison et al., 1985). $^{40}Ar/^{39}Ar$ biotite ages were determined at the Nevada Isotope Geochronology Lab and are discussed in a later section. Details of the $^{40}Ar/^{39}Ar$ procedure are provided in Appendix B.

(U-Th)/He thermochronology

(U-Th)/He ages were determined on apatite and zircon from Chapedony complex gneiss and post-metamorphic plutons as well as from Ediacaran to Cambrian rocks in the tilted crustal section of the eastern domain. These ages represent the time since the samples cooled below the He closure temperatures of apatite and zircon, which are about 70°C and 190°C, respectively (Wolf et al., 1996, Reiners et al., 2002). Apatite grains were placed in Pt tubes and heated with a Nd-YAG laser at the California Institute of Technology to extract helium, which was then analyzed by mass spectrometry (House et al., 2000). The grains were subsequently dissolved in nitric acid and analyzed with ICP-MS to determine U and Th concentrations. Zircon (U-Th)/He ages were determined using a similar procedure but utilizing a flux of lithium metaborate to facilitate the dissolution of zircon in nitric acid (Tagami et al., 2003). Details of the (U-Th)/He procedure are provided in Appendix C.

Western domain

(U-Th)/He ages were determined from gneisses at Kalut-e-Chapedony and postmetamorphic plutons at Daranjir Mountain (Table S4, Figure 2). Zircons from 0504, a sample of Chapedony gneiss, have an average (U-Th)/He age of 43.0 ± 7.8 (2σ) Ma; apatites from this sample have an age of 20.3 ± 5.8 Ma. G18, another sample of Chapedony gneiss, has a zircon (U-Th)/He age of 48.8 ± 15.6 Ma.

Zircons from samples G27 (Khoshoumi granite) and G30 (Daranjir diorite) yield (U-Th)/He ages of 40.5 ± 5.8 Ma and 40.6 ± 5.2 Ma, respectively. Apatites from these two samples have (U-Th)/He ages of 22.8 ± 3.3 and 15.4 ± 8.4 Ma, respectively.

These results suggest that both the gneisses of the Chapedony complex and the unmetamorphosed plutons cooled through the zircon He partial retention zone during middle Eocene core complex formation. The overlap, within error, of U-Pb and zircon

(U-Th)/He ages from the gneisses suggests rapid middle Eocene cooling. Subsequent cooling to ~70° C by ~20 Ma occurred at a much lower rate.

Eastern domain

The presence of an east tilted crustal section with >10 km of structural relief immediately east of the core complexes raises the issue of whether the crustal section was generated by flexural isostasy accompanying Eocene extension along a west-dipping detachment system analogous to a number of examples in the North American Cordillera (Wernicke and Axen, 1988). In the Cordilleran examples, the tilting of crustal sections in the footwalls of major normal faults usually occurs rapidly, effectively "quenching" the thermal structure that existed within the crustal section just prior to unroofing (e.g., Fitzgerald et al., 1991; Reiners et al., 2000; Stockli, 2005). If the crustal section of the eastern domain was formed by Eocene extension, an east-west horizontal transect of cooling ages across the domain would be expected to yield progressively younger ages toward the west, reaching an Eocene minimum.

A ~20 km long horizontal depth profile along Boneh-Shurow and Tashk Mountains, from unmetamorphosed CVSU near the top of the crustal section in the east to crystalline rocks at significant structural depth within the Boneh-Shurow complex to the west (Figure 2), was sampled for (U-Th)/He and $^{40}Ar/^{39}Ar$ dating to determine the age of tilting. (U-Th)/He apatite and zircon ages determined from this profile are primarily from detrital grains in sedimentary or metasedimentary rocks, and generally display a significant amount of scatter but do not vary systematically with structural position. Mean zircon

(U-Th)/He ages range from 100 to 134 Ma and overlap (using two-sigma errors) between 116 and 125 Ma. Mean apatite ages range from 17 to 20 Ma (Table S5). In contrast, $^{40}Ar/^{39}Ar$ ages determined on metamorphic biotite from six of the samples do exhibit variation with position. $^{40}Ar/^{39}Ar$ biotite ages vary from 150 to 160 Ma in structurally deeper parts of the section to 218 to 295 Ma in the upper part. As is apparent from a plot of age versus structural position (Figure 10a), the data indicate Late Jurassic tilting of the crustal section, followed by relatively uniform cooling of the entire section below ~190° C in mid-Cretaceous time, and cooling of at least the westernmost half of the section below ~70° C in latest Oligocene or early Miocene time. Late Jurassic tilting may also account for the ca. 150 Ma lower-intercept ages of zircons from the Boneh-Shurow complex (Figure 10b) since decompression accompanying rapid exhumation of these structurally deep rocks may have cracked the zircons and facilitated Pb-loss along microfractures.

DISCUSSION AND CONCLUSIONS

The region of Eocene gneisses in the Saghand area clearly contains all of the major tectonic elements known from metamorphic core complexes in the North American Cordillera. Each of the four ranges in the western domain contains a brittle fault emplacing various upper crustal assemblages on deep-seated gneisses, which is a signature observation along the 2,000 km-long belt of core complexes in North America (e.g., Davis et al., 1980; Coney, 1980; Armstrong, 1982). The structural style of younger-over-older, moderate- to low-angle faults observed in central Iran is ubiquitous in the hanging wall structure of Cordilleran detachments. A distinctive structural style of lozenge-shaped fault blocks bounded by gouge and breccia, termed *chaos structure,* has been described from a number of Cordilleran examples (Noble, 1941; Wernicke and Burchfiel, 1982; Wright and Troxel, 1984). Mylonitic gneisses are also ubiquitous in the footwalls of Cordilleran examples (e.g., Davis and Coney, 1979; Davis, 1980; Davis and Lister, 1988). In particular, where the footwalls of the Cordilleran examples are primarily granitic, as in the Sonoran Desert region, the development of L-S tectonite overprinted by chloritic brecciation (e.g., Reynolds, 1985; Spencer and Welty, 1986) bears strong similarity to the central Iran complexes. The development of thick deposits of primarily non-marine sedimentary and volcanic successions containing rock avalanche breccias, steeply tilted and juxtaposed on structurally lower rocks, referred to as supradetachment basins (e.g., Friedmann et al., 1994), are well described from most Cordilleran examples.

The topographic expression of the mountain ranges bearing the Chapedony complex has been given the special term *kalut* in the local Farsi dialect, which signifies a tendency toward having a broad, flat upland area, in contrast to the relatively narrow, cuspate ridge lines characteristic of surrounding ranges (Ramezani and Tucker, 2003). This pattern is similar to that of Cordilleran metamorphic core complexes, especially in the southwestern U. S., where domes of variably mylonitic gneisses in the footwalls of extensional detachments are expressed by a domiform topography or *turtleback* (e.g. Wright et al., 1974; Coney, 1980).

In addition to these common features, we further note that the tectonic setting of the Cordilleran examples is that of a continental or Andean type magmatic arc (Coney, 1980; Armstrong, 1982; Armstrong and Ward, 1991). The middle Eocene timeframe for the development of the Saghand area core complexes (see below) coincides with peak production of arc magmas in the Urumieh-Dokhtar, Alborz, Lut and related magmatic arcs of central Iran. The protoliths of mylonitic plutons, the undeformed plutons of the Daranjir Mountain area and volcanic strata within the supradetachment basin are all contemporaneous with the mid-Tertiary magmatic arc system of central Iran and are broadly synchronous with development of extension in the back-arc region.

Timing of extension

A summary of known (solid lines) and inferred (dashed lines) superposition relationships and relevant geochronologic data for the Khoshoumi Mountain transect is illustrated in Figure 11. Peak metamorphism (migmatization) and mylonitization of the Chapedony complex is bracketed between 44 and 49 Ma based on the oldest U-Pb zircon ages from Chapedony complex gneiss and the late-stage plutons at Daranjir Mountain. $^{40}Ar/^{39}Ar$ age determinations indicate that as late as 41 Ma, a supradetachment basin had formed in the hanging wall of the detachment. Not long after this time, the basin fill was steeply tilted and intruded by the dacite plug, which yields the same age, within uncertainties, as the biotite tuff within the basin. Given uncertainties of ca. +/- 2 Ma on both ages, the maximum time available for post tuff sedimentation, tilting, and final motion on the detachment and its hanging wall splays is 4 My. The age constraints therefore imply that mylonitization of extant igneous rock occurred between 49 and 44 Ma, and movement on the Neybaz-Chatak fault and supradetachment basin development was completed no later than 41+/-2 Ma.

Kinematics of extension

Present data from the Saghand area do not provide sufficient constraints on the magnitude and direction of extension that led to exhumation of the core complexes. The complete lithological mismatch between hanging wall and footwall of the Neybaz-Chatak detachment system suggests an amount of extension that is at least as wide as the complexes themselves, or at least 30 km. Assuming extension of this magnitude occurred over, at most, 4 My as outlined above, we obtain a minimum average horizontal extension rate of ~8 mm/yr. The 4 My timescale is quite similar to that observed for similar geochronologic constraints on Cordilleran examples (e.g., Holm and Dokka, 1993; Niemi et al., 2001; Walker et al., 1990; Wells et al., 2000; Gans and Bohrson, 1998), and the ~8 mm/yr rate is similar to those measured in both the Cordillera and the Aegean region (e.g., Kumerics et al, 2005; Ring et al., 2003).

In Cordilleran examples, the extension direction is usually indicated by three major criteria, independent of piercing points that might be observed between hanging wall and footwall. These include 1) development of extensive areas of extension-parallel mylonitization (e.g., Rehrig and Reynolds, 1980; Davis, 1980); 2) the development of extension-parallel antiforms and synforms in the detachment surface at a variety of scales (e.g., John, 1987; Spencer and Reynolds, 1989); and 3) tilt direction of hanging wall fault blocks including supradetachment basin deposits, such that the tilt direction is opposite the transport direction on the detachment fault (e.g., Davis et al., 1980; Shackelford, 1980). A fourth, perhaps less robust consideration is that in the Cordilleran examples, belts of core complex mountain ranges tend to be elongate perpendicular to the regional extension direction, as for example in the Lower Colorado River trough region of the Sonoran Desert (Spencer and Reynolds, 1989).

As detailed above, the orthogonality in the trend of lineations between Kalut-e-Chapedony and Khoshoumi Mountain, and the lack of clear cut asymmetry in shear direction make it difficult to apply the first criterion. Given the observation of significant post-Eocene deformation in the area, it is possible that the orthogonality of lineation trend is, at least in part, the result of vertical-axis rotations of the range blocks. In a paleomagnetic study of Cretaceous limestones just north of Saghand, Soffel et al. (1996) concluded that the tilt-corrected paleomagnetic pole for these strata is concordant with a modest number of other Cretaceous directions in the CEIM. We interpret this data to preclude major (>30º) differential rotation of the Neybaz Mountain-Khoshoumi Mountain area with respect to the remainder of the CEIM. Further, the continuity and general eastward dip of the Neybaz-Chatak fault along its entire length argues against major post-extensional dismemberment and vertical-axis rotation of the core complex belt, and hence we do not favor post-extensional vertical-axis rotation as an explanation for the differing trends in mylonitic lineation.

Despite the general occurrence of extension-parallel mylonites in many core complexes, it is not uncommon to observe more than one flow direction in footwall mylonites (e.g., MacCready et al., 1997). Although in some instances footwall mylonites may be interpreted as the down dip continuation of brittle simple shear on their overlying detachments (e.g., Wernicke, 1981; Lister et al., 1984), much of the mylonitic gneiss in Cordilleran and other examples is now regarded as the result of mid-crustal channel flows directed toward the area of maximum unroofing during extension (e.g., Wernicke, 1992; MacCready et al., 1997; Brun et al., 1994). Therefore, our preferred interpretation of the nearly orthogonal trends of the mylonitic lineations is that the Kalut-e-Chapedony mylonites represent eastward flow of middle crustal rocks toward the region of denudation early in the extension process, and the Khoshoumi Mountain and Neybaz Mountain mylonites, located along the southern margin of the extended region, record northerly flow toward the same region.

The criterion of antiforms and synforms is also difficult to evaluate. Neybaz and Khoshoumi Mountains and Kalut-e-Chatak are elongate roughly east-west, but Kalut-e-Chapedony is slightly elongate north-south. On the whole, this would appear to suggest east-west extension, but the topographic pattern is in general not as regular as that for the best Cordilleran examples. Furthermore, given the evidence for post-extensional folding in the area, the morphology of the core complex ranges could relate more to an episode of Neogene folding than to the episode of Eocene extension.

As regards hanging wall tilt direction, the supradetachment basin deposits along the northeast flank of Khoshoumi Mountain are tilted ~ESE, implying WNW displacement on the detachment system. As with the other criteria, tilt direction in Cordilleran examples is not always opposite the direction of slip on the fault, and in several instances has been shown to be either in the same direction as slip (e.g., Wernicke, 1985), or significantly oblique to the extension direction (e.g., Hodges et al., 1989).

Although further work is clearly required to resolve the issue, the NNE trend of the belt of core complexes, the ESE tilt direction of the supradetachment basin at Khoshoumi Mountain, the ~E-W elongation direction of 3 of the 4 core complex ranges, and the WSW trend of mylonitic lineation at Kalut-e-Chapedony suggest an overall E-W extension direction, with transport on the detachment top to the west. We interpret the northerly lineation direction at Khoushoumi and Neybaz Mountains to be the result of extension-normal flow of deep-crustal rocks from unextended areas in the south toward the region of maximum unroofing to the north.

Cretaceous and Miocene (U-Th)/He cooling ages

Although the eastern and western domains both yield Miocene apatite ages, the Cretaceous zircon cooling ages from the eastern domain contrast strongly with the Eocene zircon cooling ages from the western domain. As discussed above, the $^{40}Ar/^{39}Ar$ biotite ages and uniformity of (U-Th)/He apatite and zircon ages across the crustal section indicates that tilting and rapid cooling, perhaps due to contactional deformation in the region, occurred in the Late Jurassic. As noted above, a regional angular unconformity separates Albian(?) to Cenomanian strata from Middle Jurassic and older rocks.

Miocene (U-Th)/He apatite ages obtained from both the western and eastern domains suggest a period of exhumation that postdates extension by approximately 20 My. Assuming a mid-Tertiary geothermal gradient of 30º C/km, appropriate for continental arc terrain, and a mean surface temperature of 10º C, a pre-Miocene depth of ~2000 m is indicated by these ages. We interpret these ages to reflect cooling related to ~N-S shortening of the region, as suggested by the folding of Neogene strata near Saghand as discussed above (Figure 4b). The development of a major early Miocene east-west trending fold raises the question of whether this deformation is related to the Arabia-Eurasia collision. According to the palinspastic and plate tectonic arguments presented by McQuarrie et al. (2003), 20 Ma is the earliest possible time of collision between Arabia and central Iran. If the age of initial collision is closer to 10 Ma as preferred by McQuarrie et al., then the fold would represent shortening in an Andean-type setting and would suggest a pre-collisional transition from extension to compression in the overriding plate at some time between ~40 and ~20 Ma as suggested by Vincent et al. (2005) based on stratigraphic data from Azerbaijan. Such a transition occurred there near the end of the Eocene, which they interpreted as supporting previous suggestions that the initial collision occurred at ca. 40 Ma. Although data collected during this study only indirectly bear on this issue, the simple plate tectonic and palinspastic arguments indicate that at 40 Ma there was >1000 km of separation between central Iran and the Zagros Mountains. Clearly the details of how various Neo-Tethyan continental fragments may have interacted with one another are at issue, but wholesale arrival of the Arabian subcontinent against contiguous, south Asian continental crust (i.e., the broadest possible definition of the “initial collision” of Arabia with Eurasia, as opposed to the collision of intra-Tethyan continental fragments) by 40 Ma is unlikely.

Regional significance

In addition to the core complexes exposed near Saghand, core complexes have also been reported in northwest (Stockli et al., 2004) and northeast (Hassanzadeh et al., 2005) Iran (Figure 1). Existing geologic maps (Thiele et al., 1967; Tillman et al., 1981) and satellite image reconnaissance strongly suggest the presence of a fourth Iranian core complex in southwest Iran near the town of Golpaygan (Figure 1). Available thermochronologic data indicate that the Iranian core complexes may span a range in age from late Cretaceous to early Miocene. Prior to these reports, there were no known regions of significant Tertiary extension within the Tethysides between the Bitlis suture in eastern Turkey and the western Himalyan syntaxis. The widespread occurrence of core complexes in Iran demonstrates that core complex development has affected every major segment of the Tethysides (Figure 12 and Table 1).

Formation of the Cretaceous to Cenozoic core complexes of the Alpine-Himalayan orogen is usually attributed to either back-arc extension associated with rapid subduction or “slab rollback,” such as in the Tyrrhenian basin (e.g., Royden, 1993), or to large gradients in gravitational potential energy within the lithosphere resulting from localized crustal thickening (e.g., Dewey, 1988). The former has been invoked by some authors to account for the numerous core complexes of Spain, western Turkey and the Tyrrhenian and Aegean Seas (e.g., Brunet et al., 2000; Buick, 1991; Dinter, 1998; Lonergan and

White, 1997; Okay and Satir, 2000; Thomson et al., 1999), while other authors have suggested that the latter process is responsible for extensional structures in Spain, the Himalayas and eastern China (Platt and Vissers, 1989; Burchfiel et al., 1992; Davis et al., 2002). Extension in the eastern Alps has been ascribed to a combination of gravitational collapse and tectonic escape (e.g., Ratschbacher et al., 1991a, b). Extension in the Saghand region long predated any intracontinental shortening resulting from direct contact between Arabia and Eurasia, which argues against core complex formation as the result of thickened crust or the eastward extrusion of the CEIM (Figure 1). The extension direction appears to be oblique, or perhaps sub-parallel, to the Urumieh-Dokhtar magmatic arc, but perpendicular to the north-south trending Lut segment of the Iranian arc, currently ~200 km east of the Saghand area. Kazmin et al. (1986) conclude that volcanism within the Lut arc resulted from the westward subduction of oceanic crust separating the CEIM from Afghanistan, as shown on the paleogeographic reconstructions of Dercourt et al. (1986). Eocene extension within the Saghand region therefore may be a pre-collisional back-arc spreading event associated with the eastern segment of the Iranian arcs.

ACKNOWLEDGEMENTS

We would like to thank the University of Tehran Research Council for their support of this project and Ahmad Reza Malekpour for his efforts in the field. Ken Farley, Rebecca Flowers, and Lindsey Hedges provided assistance with the (U-Th)/He analyses. Bernard Guest and Kevin Mahan conducted informal reviews of a pre-submission version of the manuscript. Kevin Mahan also offered helpful advice in microstructural analysis.

Comments from Mark Allen, David Foster and Uwe Ring greatly improved the manuscript. Financial support for this project was provided by the Caltech Tectonics Observatory and NSF grant EAR-0511054.

REFERENCES

Alavi, M., 1991, Sedimentary and structural characteristics of the Paleo-Tethys remnants in northeastern Iran: Geological Society of America Bulletin, v. 103, p. 983-992.

Argles, T.W., and Edwards, M.A., 2002, First evidence for high-grade, Himalyan-age synconvergent extension recognized within the western syntaxis; Nanga Parbat, Pakistan: Journal of Structural Geology, v. 24, p. 1327-1344.

Armstrong, R.L., 1982, Cordilleran metamorphic core complexes; from Arizona to southern Canada: Annual Review of Earth and Planetary Sciences, v.10, p.129-154.

Armstrong, R.L, and Ward, P.L., 1991, Evolving geographic patterns of Cenozoic magmatism in the North American Cordillera; the temporal and spatial association of magmatism and metamorphic core complexes: Journal of Geophysical Research, B, Solid Earth and Planets, v.96, p. 13201-13224.

Axen, G.J., Bartley, J.M., and Selverstone, J., 1995, Structural expression of a rolling hinge in the footwall of the Brenner Line normal fault, eastern Alps: Tectonics, v. 14, p. 1380-1392.

Axen, G.J., Lam, P.S., Grove, M., Stockli, D.F., and Hassanzadeh, J., 2001, Exhumation of the west-central Alborz Mountains, Iran, Caspian subsidence, and collision-related tectonics: Geology, v. 29, p. 559-562.

Brun, J.-P., Sokoutis, D., and van den Driessche, J., 1994, Analogue modeling of detachment fault systems and core complexes: Geology, v. 22, p. 319-322.

Brunel, M., Arnaud, N., Tapponnier, P., Pan, Y., and Wang, Y., 1994, Kongur Shan normal fault: type example of mountain building assisted by extension (Karakoram fault, eastern Pamir): Geology, v. 22, p. 707-710.

Brunet, C., Monie, P., Jolivet, L., and Cadet, J.-P., 2000, Migration of compression and extension in the Tyrrhenian Sea, insights from $^{40}Ar/^{39}Ar$ ages on micas along a transect from Corsica to Tuscany: Tectonophysics, v. 321, p. 127-155.

Buick, I.S., 1991, The late Alpine evolution of an extensional shear zone, Naxos, Greece: Journal of the Geological Society, London, v. 148, p. 93-103.

Burchfiel, B.C., Chen, Z., Hodges, K.V., Yuping, L., Royden, L.H., Changrong, D., and Jiene, X., 1992, The South Tibetan detachment system, Himalayan Orogen; extension contemporaneous with and parallel to shortening in a collisional mountain belt: GSA Special Paper, v. 269, 41 p.

Caby, R., Hammor, D., and Delor, C., 2001, Metamorphic evolution, partial melting and Miocene exhumation of lower crust in the Edough metamorphic core complex, west Mediterranean orogen, eastern Algeria: Tectonophysics, v. 342, p. 239-273.

Carmignani, L., Decandia, F.A., Fantozzi, P.L., Lazzarotto, A., Liotta, D., and Meccheri, M., 1994, Tertiary extensional tectonics in Tuscany (Northern Apennines, Italy): Tectonophysics, v. 238, p. 295-315.

Carmignani, L., and Roy, K., 1990, Crustal extension in the Northern Apennines; the transition from compression to extension in the Alpi Apuane core complex: Tectonics, v. 9, p. 1275-1303.

Chen, Z., Liu, Y., Hodges, K.V., Burchfiel, B.C., Royden, L.H., and Deng, C., 1990, The Kangmar Dome; a metamorphic core complex in southern Xizang (Tibet): Science, v. 250, p. 1552-1556.

Coney, P.J., 1980, Cordilleran metamorphic core complexes; an overview: Geological Society of America Memoir, no. 153, p. 7-31.

Davis, G.A., Anderson, J.L., Frost, E.G., and Shackelford, T.J., 1980, Mylonitization and detachment faulting in the Whipple-Buckskin-Rawhide Mountains terrane, southeastern

California and western Arizona: Geological Society of America Memoir, no. 153, p. 79-129.

Davis, G.A., Darby, B.J., Yadong, Z., and Spell, T.L., 2002, Geometric and temporal evolution of an extensional detachment fault, Hohhot metamorphic core complex, Inner Mongolia, China: Geology, v. 30, p. 1003-1006.

Davis, G.A., and Lister, G.S., 1988, Detachment faulting in continental extension; perspectives from the Southwestern U.S. Cordillera, *in* Clark, S.P., Burchfiel, B.C., Suppe, J., Processes in continental lithospheric deformation, Geological Society of America Special Paper, v. 218, p.133-159.

Davis, G.H, 1980, Structural characteristics of metamorphic core complexes, southern Arizona: Geological Society of America Memoir, no. 153, p. 35-77.

Davis, G.H., and Coney, P.J., 1979, Geologic development of the Cordilleran metamorphic core complexes: Geology, v. 7, p. 120-124.

Dercourt, J., L. P. Zonenshain, L. E. Ricou, V. G. Kazmin, X. Le Pichon, A. L. Knipper, C. Grandjacquet, I. M. Sbortshikov, J. Geyssant, C. Lepvrier, D. H. Pechersky, J. Boulin, J.-C. Sibuet, L. A. Savostin, O. Sorokhtin, M. Westphal, M. L. Bazhenov, J. P. Lauer, and B. Biju-Duval, 1986, Geological evolution of the Tethys belt from the Atlantic to the Pamirs since the Lias: Tectonophysics, v. 123, p. 241–315.

Dewey, J.F., 1988, Extensional collapse of orogens: Tectonics, v. 7, p. 1123-1139.

Dinter, D.A., 1998, Late Cenozoic extension of the Alpine collisional orogen, northeastern Greece: origin of the north Aegean basin: GSA Bulletin, v. 110, p. 1208-1230.

Dinter, D.A., Macfarlane, A., Hames, W., Isachsen, C., Bowring, S., and Royden, L., 1995, U-Pb and $^{40}Ar/^{39}Ar$ geochronology of the Symvolon granodiorite: Implications for the thermal and structural evolution of the Rhodope metamorphic core complex, northeastern Greece: Tectonics, v. 14, p. 886-908.

Fitzgerald, P.G., Fryxell, J.E, and Wernicke, B.P., 1991, Miocene crustal extension and uplift in southeastern Nevada; constraints from fission track analysis: Geology, v. 19, p. 1013-1016.

Forster, H., Fesefeldt, K., and Kursten, M., 1972, Magmatic and orogenic evolution of the central Iranian volcanic belt: 24th International Geologic Congress, Section 2, p. 198-210.

Fournier, M., Jolivet, L., Goffe, B., and Dubois, R., 1991, Alpine Corsica metamorphic core complex: Tectonics, v. 10, p. 1173-1186.

Friedmann, S.J., Davis, G.A., Fowler, T.K., Brudos, T., Parke, M., Burbank, D.W., and Burchfiel, B.C., 1994, Stratigraphy and gravity-glide elements of a Miocene supradetachment basin, Shadow Valley, East Mojave Desert *in* McGill, S.F. and Ross, T.M., Geological investigations of an active margin: Geological Society of America, Cordilleran Section, Annual Meeting, Guidebook., v. 27, p. 302-318.

Fugenschuh, B., and Schmid, S.M., 2005, Age and significance of core complex formation in a very curved orogen: evidence from fission track studies in the South Carpathians (Romania): Tectonophysics, v. 404, p. 33-53.

Gans, P.B., and Bohrson, W.A., 1998, Suppression of volcanism during rapid extension in the Basin and Range Province, United States: Science, v. 279, p. 66-68.

Gautier, P., and Brun, J.-P., 1994, Crustal-scale geometry and kinematics of late-orogenic extension in the central Aegean (Cyclades and Evvia Island): Tectonophysics, v. 238, p. 399-424.

Gessner, K., Ring, U., Johnson, C., Hetzel, R., Passchier, C.W., and and Gungor, T., 2001, An active bivergent rolling-hinge detachment system: central Menderes metamorphic core complex in western Turkey: Geology, v. 29, p. 611-614.

Grassl, H., Neubauer, F., Millahn, K., and Weber, F., 2004, Seismic image of the deep crust at the eastern margin of the Alps (Austria): indications for crustal extension in a convergent orogen: Tectonophysics, v. 380, p. 105-122.

Haghipour, A., 1977a, Geological map of the Biabanak-Bafq area: Geological Survey of Iran, scale 1:500,000.

Haghipour, A., 1977b, Geological map of the Posht-e-Badam area: Geological Survey of Iran, scale 1:100,000.

Haghipour, A., and Aghanabati, A. (compilers), 1985, Geological map of Iran, Ministry of Mines and Metals, Geological Survey of Iran.

Haghipour, A., Valeh, N., Pelissier, G., and Davoudzadeh, 1977, Explanatory text of the Ardekan quadrangle map, Geological Survey of Iran, Geological Quadrangle H8, 114 p.

Harrison, T.M., Duncan, I., and McDougal, I., 1985, Diffusion of ^{40}Ar in biotite: Temperature, pressure and compositional effects: Geochimica et Cosmochimica Acta, v. 49, p. 2461-2468.

Hassanzadeh, J., Ghazi, A.M., Axen, G., and Guest, B., 2002, Oligomiocene mafic-alkaline magmatism in north and northwest of Iran: evidence for the separation of the

Alborz from the Urumieh-Dokhtar magmatic arc: Geological Society of America Abstracts with Programs, v. 34, no. 6, p. 331.

Hassanzadeh, J., Malekpour, A., Grove, M., Axen, G.J., Horton, B.K., Stockli, D.F., Farley, K., Schmitt, A.K., Mohajjel, M., and Ghazi, A.M., 2005, Biarjmand metamorphic core complex; new evidence for Late Cretaceous-Paleocene extensional tectonics along the northern margin of central Iranian Plateau: Geological Society of America Abstracts with Programs, v. 37, no. 7, p. 71.

Hippertt, J., and Tohver, E., 1999, On the development of zones of reverse shearing in mylonitic rocks: Journal of Structural Geology, v.21, p. 1603-1614.

Hodges, K.V., McKenna, L.W., Stock, J., Knapp, J., Page, L., Sternlof, K., Wuest, G., and Walker, J.D., 1989, Evolution of extensional basins and basin and range topography west of Death Valley, California: Tectonics, v. 8, p. 453-467.

Holm, D.K., and Dokka, R.K., 1993, Interpretation and tectonic implications of cooling histories; an example from the Black Mountains, Death Valley extended terrane, California: Earth and Planetary Science Letters, v. 116, p.63-80.

House, M.A., Farley, K.A., Stockli, D., 2000, Helium chronometry of apatite and titanite using Nd-YAG laser heating: Earth and Planetary Science Letters, v. 183, p. 365-368.

Hubbard, M.S., Spencer, D.A., and West, D.P., 1995, Tectonic exhumation of the Nanga Parbat massif, northern Pakistan: Earth and Planetary Science Letters, v. 133, p. 213-225.

Jaffey, A. H., Flynn, K. F., Glendenin, L. E., Bentley, W. C., and Essling, A. M., 1971, Precision Measurement of Half-Lives and Specific Activities of ^{235}U and ^{238}U: Physical Review C, v. 4, no. 5, p. 1889-1906.

Janak, M., Plasienka, D., Frey, M., Cosca, M., Schmidt, S.T., Luptak, B., and Meres, S., 2001, Cretaceous evolution of a metamorphic core complex, the Veporic unit, Western Carpathians (Slovakia): P-T conditions and in situ $^{40}Ar/^{39}Ar$ UV laser probe dating of metapelites: Journal of Metamorphic Geology, v. 19, p. 197-216.

John, B.E., 1987, Structural and intrusive history of the Chemehuevi Mountains area, southeastern California and western Arizona: Doctoral thesis, University of California, Santa Barbara, 344 p.

Jolivet, L., Faccenna, C., Goffe, B., Mattei, M., Rossetti, F., Brunet, C., Storti, F., Funiciello, R., Cadet, J.P., d'Agostino, N., and Parra, T., 1998, Midcrustal shear zones in postorogenic extension: example from the northern Tyrrhenian Sea: Journal of Geophysical Research, v. 103, p. 12123-12160.

Junlai, L., Davis, G.A., Zhiyong, L., and Fuyuan, W., 2005, The Liaonan metamorphic core complex, Southeastern Liaoning Province, North China: a likely contributor to

Cretaceous rotation of Eastern Liaoning, Korea and contiguous areas: Tectonophysics, v. 407, p. 65-80.

Kargaran, F., Neubauer, F., Genser, J., and Houshmandzadeh, A., 2006, The Eocene Chapedony metamorphic core complex in central Iran: preliminary structural results: European Geosciences Union Geophysical Research Abstracts, v. 8.

Kazmin, V.G., Sbortshikov, I.M., Ricou, L.-E., Zonenshain, L.P., Boulin, J., and Knipper, A.L., 1986, Volcanic belts as markers of the Mesozoic-Cenozoic active margin of Eurasia: Tectonophysics, v. 123, p. 123-152.

Kounov, A., Seward, D., Bernoulli, D., Burg, J.-P., and Ivanov, Z., 2004, Thermotectonic evolution of an extensional dome: the Cenozoic Osogovo-Lisets core complex (Kraishte zone, western Bulgaria): Geologische Rundschau, v. 93, p. 1008-1024.

Kumerics, C., Ring, U., Brichau, S., Glodny, J., and Monie, P., 2005, The extensional Messaria shear zone and associated brittle detachment faults, Aegean Sea, Greece: Journal of the Geological Society, London, v. 162, p. 701-721.

Lee, J., Miller, E.L., and Sutter, J.F., 1987, Ductile strain and metamorphism in an extensional tectonic setting: a case study from the northern Snake Range, Nevada, USA *in* Coward, M.P., Dewey, J.F., and Hancock P.L., eds., Continental extensional tectonics, Geological Society Special Publication No. 28, p. 267-298.

Lee, J., Hacker, B.R., Dinklage, W.S., Wang, Y., Gans, P., Calvert, A., Wan, J., Chen, W., Blythe, A.E., and McClelland, W., 2000, Evolution of the Kangmar Dome, southern Tibet: structural, petrologic and thermochronologic constraints, Tectonics, v. 19, p. 872-895.

Lee, J., Hacker, B., and Wang, Y., 2004, Evolution of north Himalyan gneiss domes: structural and metamorphic studies in Mabja Dome, southern Tibet: Journal of Structural Geology, v. 26, p. 2297-2316.

Lee, J., and Lister, G.S., 1992, Late Miocene ductile extension and detachment faulting, Mykonos, Greece: Geology (Boulder), v. 20, p. 120-124.

Lehrmann, D. J., Ramezani, J., Bowring, S. A., Martin, M. W., Montgomery, P., Enos, P., Payne, J. L., Orchard, M. J., Wang, H., and Wei, J., 2006, Timing of recovery from the end-Permian extinction; geochronologic and biostratigraphic constraints from south China: Geology (Boulder), v. 34, no. 12, p. 1053-1056.

Lister, G.S., Banga, G., and Feenstra, A., 1984, Metamorphic core complexes of Cordilleran type in the Cyclades, Aegean Sea, Greece: Geology (Boulder), v. 12, p. 221-225.

Lonergan, L., and White, N., 1997, Origin of the Betic-Rif mountain belt: Tectonics, v. 16, p. 504-522.

Ludwig, K. R., 1980, Calculation of uncertainties of U-Pb isotope data: Earth and Planetary Science Letters, v. 46, no. 2, p. 212-220.

MacCready, T., Snoke, A.W., Wright, J.E., and Howard, K.A., 1997, Mid-crustal flow during Tertiary extension in the Ruby Mountains core complex, Nevada: Geological Society of America Bulletin, v. 109, p. 1576-1594.

Mancktelow, N.S., and Pavlis, T.L., 1994, Fold-fault relationships in low-angle detachment systems: Tectonics, v. 13, p. 668-685.

McQuarrie, N., Stock, J.M., Verdel, C., and Wernicke, B.P., 2003, Cenozoic evolution of Neotethys and implications for the causes of plate motions: Geophysical Research Letters, v. 30, 2036, doi:10.1029/2003GL017992.

Niemi, N.A., Wernicke, B.P., Brady, R.J., Saleeby, J.B., and Dunne, G.C., 2001, Distribution and provenance of the middle Miocene Eagle Mountain Formation, and implications for regional kinematic analysis of the Basin and Range Province: Geological Society of America Bulletin, v. 113, p. 419-442.

Noble, L.F., 1941, Structural features of the Virgin Spring area, Death Valley, California: Geological Society of America Bulletin, v. 52, p. 941-999.

Okay, A.I., and Satir, M., 2000, Coeval plutonism and metamorphism in a latest Oligocene metamorphic core complex in northwest Turkey: Geological Magazine, v. 137, p. 495-516.

Passchier, C.W., and Trouw, R.A.J., 2005, Microtectonics: Berlin, Springer, 366 p.

Platt, J.P., and Compagnoni, R., 1990, Alpine ductile deformation and metamorphism in a Calabrian basement nappe (Aspromonte, South Italy): Eclogae Geologicae Helvetiae, v. 83, p. 41-58.

Platt, J.P., and Vissers, R.L.M., 1989, Extensional collapse of thickened continental lithosphere: a working hypothesis for the Alboran sea and Gibraltar arc: Geology, v. 17, p.540-543.

Platzman, E., and Platt, J.P., 2004, Kinematics of a twisted core complex: Oblique axis rotation in an extended terrane (Betic Cordillera, southern Spain): Tectonics, v. 23, TC6010, doi:10.1029/2003TC001549.

Ramezani, J., and Tucker, R.D., 2003, The Saghand region, central Iran: U-Pb geochronology, petrogenesis and implications for Gondwana tectonics: American Journal of Science, v. 303, p. 622-665.

Ratschbacher, L., Behrmann, J.H., and Pahr, A., 1990, Penninic windows at the eastern end of the Alps and their relation to the intra-Carpathian basins: Tectonophysics, v. 172, p. 91-105.

Ratschbacher, L., Merle, O., Davy, P., and Cobbold, P., 1991a, Lateral extrusion in the eastern Alps, part I, boundary conditions and experiments scaled for gravity: Tectonics, v. 10, p. 245-256.

Ratschbacher, L., Frisch, W., and Linzer, H.-G., 1991b, Lateral extrusion in the eastern Alps, part II, structural analysis: Tectonics, v. 10, p. 257-271.

Rehrig, W.A., and Reynolds, S.J., 1980, Geologic and geochronologic reconnaissance of a northwest-trending zone of metamorphic core complexes in southern and western Arizona: Geological Society of America Memoir, no. 153, p. 131-157.

Reiners, P.W., Brady, R., Farley, K.A., Fryxell, J.E., Wernicke, B., and Lux, D., 2000, Helium and argon thermochronometry of the Gold Butte Block, South Virgin Mountains, Nevada: Earth and Planetary Science Letters, v. 178, p. 315-326.

Reiners, P.W., Farley, K.A., and Hickes, H.J., 2002, He diffusion and (U-Th)/He thermochronometry of zircon; initial results from Fish Canyon Tuff and Gold Butte: Tectonophysics, v. 349, p. 297-308.

Renne, P.R., Swisher, C.C., Deino, A.L., Karner, D.B., Owens, T., and DePaolo, D.J., 1998, Intercalibration of Standards, Absolute Ages and Uncertainties in $^{40}Ar/^{39}Ar$ Dating: Chemical Geology (Isotope Geoscience Section), v. 145 (1-2), p. 117-152.

Reynolds, S.J., 1985, Geology of the South Mountains, central Arizona: Arizona Bureau of Geology and Mineral Technology, Geological Survey Branch, Bulletin 195, 61 p.

Ring, U., and Collins, A.S., 2005, U-Pb SIMS dating of synkinematic granites: timing of core-complex formation in the northern Anatolide belt of western Turkey: Journal of the Geological Society, London, v. 162, p. 289-298.

Ring, U., Thomson, S.N., and Brocker, M., 2003, Fast extension but little exhumation: the Vari detachment in the Cyclades, Greece: Geological Magazine, v. 140, p. 245-252.

Royden, L.H., 1993, Evolution of retreating subduction boundaries formed during continental collision: Tectonics, v. 12, p. 629-638.

Schmid, S.M., Berza, T., Diaconescu, V., Froitzheim, N., and Fugenschuh, B., 1998, Orogen-parallel extension in the Southern Carpathians: Tectonophysics, v. 297, p. 209-228.

Schoene, B., Crowley, J. L., Condon, D. J., Schmitz, M. D., and Bowring, S. A., 2006, Reassessing the uranium decay constants for geochronology using ID-TIMS U–Pb data: Geochimica et Cosmochimica Acta, v. 70, p. 426-445.

Sengor, A.M.C., 1987, Tectonics of the Tethysides; orogenic collage development in a collisional setting: Annual Review of Earth and Planetary Sciences, v. 15, p. 213-244.

Sengor, A.M.C., and Natal'in, B.A., 1996, Paleotectonics of Asia: fragments of a synthesis, *in* Yin, A., and Harrison, M., The tectonic evolution of Asia: Cambridge University Press, p.486-640.

Shackelford, T.J., 1980, Tertiary tectonic denudation of a Mesozoic-early Tertiary(?) gneiss complex, Rawhide Mountains, western Arizona: Geology, v. 8, p.190-194.

Soffel, H.C., Davoudzadeh, M., Rolf, C., and Schmidt, S., 1996, New palaeomagnetic data from central Iran and a Triassic palaeoreconstruction, Geologische Rundschau, v. 85, p. 293-302.

Spencer, J.E., and Reynolds, S.J., 1989, Middle Tertiary tectonics of Arizona and adjacent areas: Arizona Geological Society Digest, v. 17, p. 539-574.

Spencer, J.E., and Welty, J.W., 1986, Possible controls of base- and precious-metal mineralization associated with Tertiary detachment faults in the lower Colorado River trough, Arizona and California: Geology, v. 14, p. 195-198.

Stockli, D.F., 2005, Application of low-temperature thermochronometry to extensional tectonic settings: Reviews in Mineralogy and Geochemistry, v. 58, p.411-448.

Stockli, D.F., Hassanzadeh, J., Stockli, L.D., Axen, G.J., Walker, J.D., and Dewane, T.J., 2004, Structural and geochronological evidence for Oligo-Miocene intra-arc low-angle detachment faulting in the Takab-Zanjan area, NW Iran: Geological Society of America Abstracts with Programs, v. 36, no. 5, p. 319.

Stöcklin, J., 1968, Structural history and tectonics of Iran: a review: AAPG Bulletin, v. 52, p. 1229-1258.

Tagami, T., Farley, K.A., and Stockli, D.F., 2003, (U-Th)/He geochronology of single zircon grains of known Tertiary eruption age: Earth and Planetary Science Letters, v. 207, p. 57-67.

Takin, M., 1972, Iranian geology and continental drift in the Middle East: Nature, v.235, p.147-150.

Thiele, O., Alavi, M., Assefi, R., Hushmand-zadeh, A., Sayed-Emami, K., and Zahedi, M., 1967, Geological map of Golpaygan: Geological Survey of Iran, scale 1:250,000.

Thomson, S.N., 1994, Fission track analysis of the crystalline basement rocks of the Calabrian Arc, southern Italy; evidence of Oligo-Miocene late-orogenic extension and erosion: Tectonophysics, v. 238, p. 331-352.

Thomson, S.N., Stoeckhert, B., and Brix, M.R., 1999, Miocene high-pressure metamorphic rocks of Crete, Greece; rapid exhumation by buoyant escape, *in* Ring, U., Brandon, M.T., Lister, G.S., and Willett, S.D., eds., Exhumation processes: normal faulting, ductile flow and erosion: Geological Society Special Publications, v. 154, p. 87-107.

Tillman, J.E., Poosti, A., Rossello, S., and Eckert, A., 1981, Structural evolution of Sanandaj-Sirjan Ranges near Esfahan, Iran: AAPG Bulletin, v. 65, p. 674-687.

Valeh, N., and Haghipour, A., 1970, Geological map of Ardekan: Geological Survey of Iran, scale 1:250,000.

van Hinsbergen, D.J.J., and Meulenkamp, J.E., 2006, Neogene supradetachment basin development on Crete (Greece) during exhumation of the South Aegean core complex: Basin Research, v. 18, p. 103-124.

Vincent, S.J., Allen, M.B., Ismail-Zadeh, A.D., Flecker, R, Foland, K.A., and Simmons, M.D., 2005, Insights from the Talysh of Azerbaijan into the Paleogene evolution of the south Caspian region: Geological Society of America Bulletin, v. 117, p. 1513-1533.

Walker, J.D., Bartley, J.M., and Glazner, A.F., 1990, Large-magnitude Miocene extension in the central Mojave Desert; implications for Paleozoic to Tertiary paleogeography and tectonics: Journal of Geophysical Research, B, Solid Earth and Planets, v. 95, p. 557-569.

Wallis, S.R., Platt, J.P., and Knott, S.D., 1993, Recognition of syn-convergence extension in accretionary wedges with examples from the Calabrian Arc and the Eastern Alps: American Journal of Science, v. 293, p. 463-494.

Wawrzenitz, N., and Krohe, A., 1998, Exhumation and doming of the Thasos metamorphic core complex (S Rhodope, Greece): structural and geochronological constraints: Tectonophysics, v. 285, p. 301-332.

Wawrzyniec, T.F., Selverstone, J., and Axen, G.J., 2001, Styles of footwall uplift along the Simplon and Brenner normal fault systems, central and Eastern Alps: Tectonics, v. 20, p. 748-770.

Wells, M.L., Snee, L.W., and Blythe, A.E., 2000, Dating of major normal fault systems using thermochronology; an example from the Raft River detachment, Basin and Range, Western United States: Journal of Geophysical Research, B, Solid Earth and Planets, v.105, p.16303-16327.

Wernicke, B., 1981, Low-angle normal faults in the Basin and Range Province; nappe tectonics in an extending orogen: Nature, v. 291, p. 645-648.

Wernicke, B., 1985, Uniform-sense normal simple shear of the continental lithosphere: Canadian Journal of Earth Sciences, v. 22, p. 108-125.

Wernicke, B., 1992, Cenozoic extensional tectonics of the U.S. Cordillera, *in* Burchfiel, B.C., Lipman, P.W., and Zoback, M.L., The Cordilleran Orogen; conterminous U.S., p. 553-581.

Wernicke, B., and Axen, G.J., 1988, On the role of isostasy in the evolution of normal fault systems: Geology, v. 16, p. 848-851.

Wernicke, B., and Burchfiel, B.C., 1982, Modes of extensional tectonics: Journal of Structural Geology, v. 4, p. 105-115.

Whitney, D.L., and Dilek, Y., 1997, Core complex development in central Anatolia, Turkey: Geology, v. 25, p. 1023-1026.

Wolf, R.A., Farley, K.A., Silver, L.T., 1996, Helium diffusion and low-temperature thermochronometry of apatite: Geochimica et Cosmochimica Acta, v. 60, p. 4231-4240.

Wright, L.A., Otton, J.K., and Troxel, B.W., 1974, Turtleback surfaces of Death Valley viewed as phenomena of extensional tectonics: Guidebook; Death Valley region, California and Nevada, p. 79-80

Wright, L.A., and Troxel, B.W., 1984, Geology of the northern half of the Confidence Hills 15-minute Quadrangle, Death Valley region, eastern California; the area of the Amargosa chaos: Map Sheet - California Division of Mines and Geology, v.34, 31 p.

Yin, A., Harrison, T.M., Murphy, M.A., Grove, M., Nie, S., Ryerson, F.J., Feng, W.X., and Chen, Z.L., 1999, Tertiary deformation history of southeastern and southwestern Tibet during the Indo-Asian collision: GSA Bulletin, v. 111, p.1644-1664.

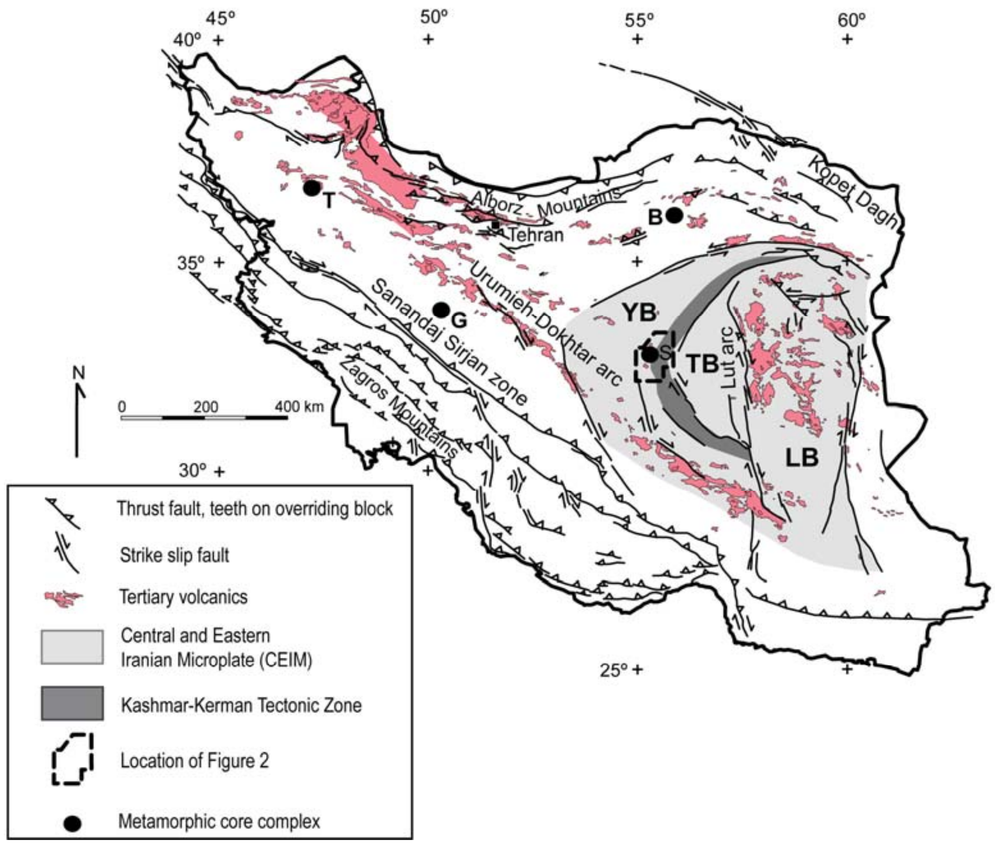

Figure 1. Distribution of Tertiary volcanic rocks, major faults (modified from Haghipour and Aghanabati, 1985) and known or suspected metamorphic core complexes in Iran. The location of the Saghand region is outlined within the Yazd Block of the Central Iranian Microcontinent. Abbreviations: B=Biarjmand core complex (Hassanzadeh et al., 2005), G=Golypaygan core complex (Thiele et al., 1967), S=Saghand core complex (this paper), T=Takab-Zanjan core complex (Stockli et al., 2004), LB=Lut Block, TB=Tabas Block, YB=Yazd Block

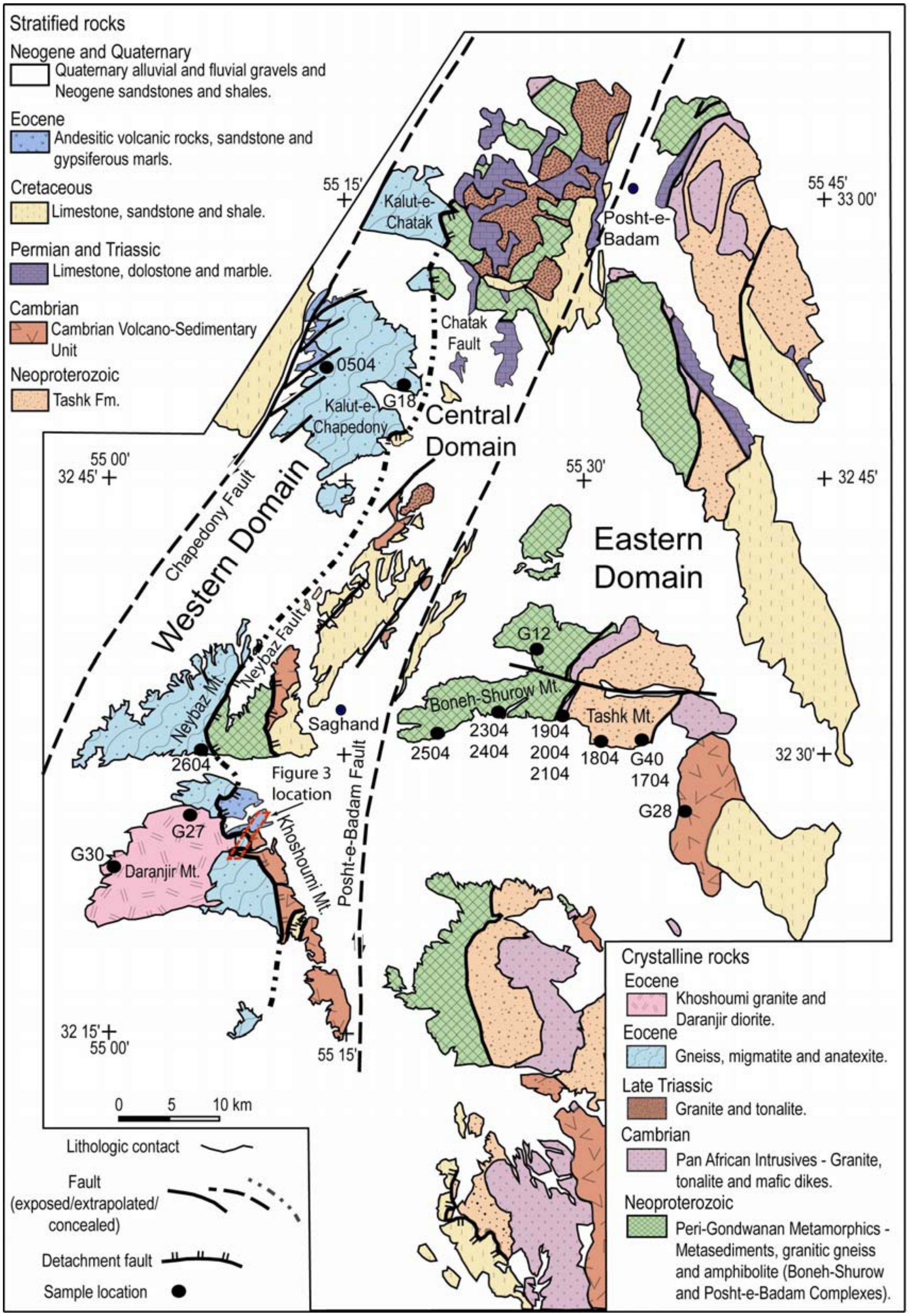

Figure 2. Geologic map of the Saghand area, modified from Ramezani and Tucker (2003).

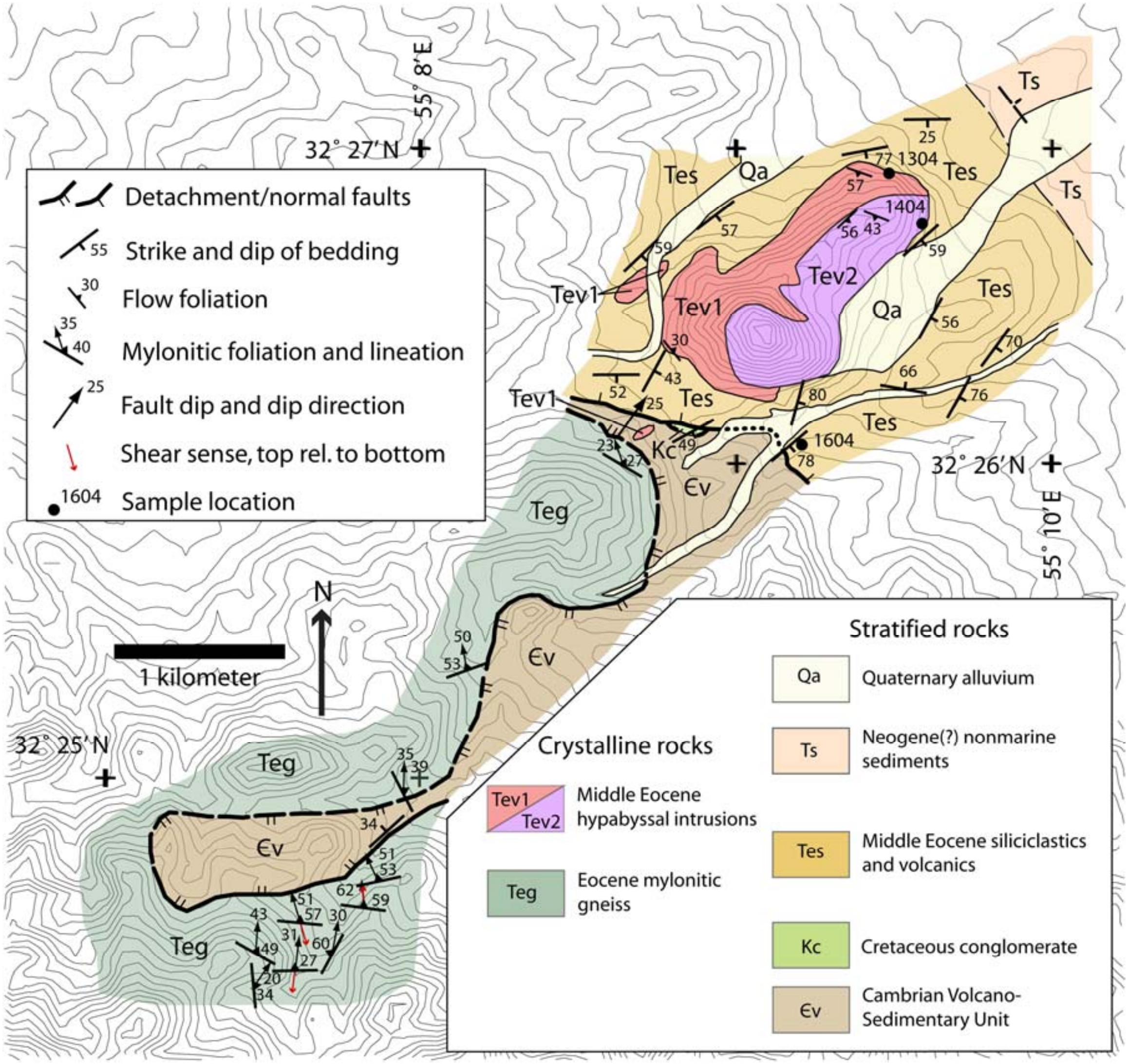

Figure 3. Geologic map of a portion of the east side of Khoushoumi Mountain showing $^{40}Ar/^{39}Ar$ sampling locations. See Figure 2 for location.

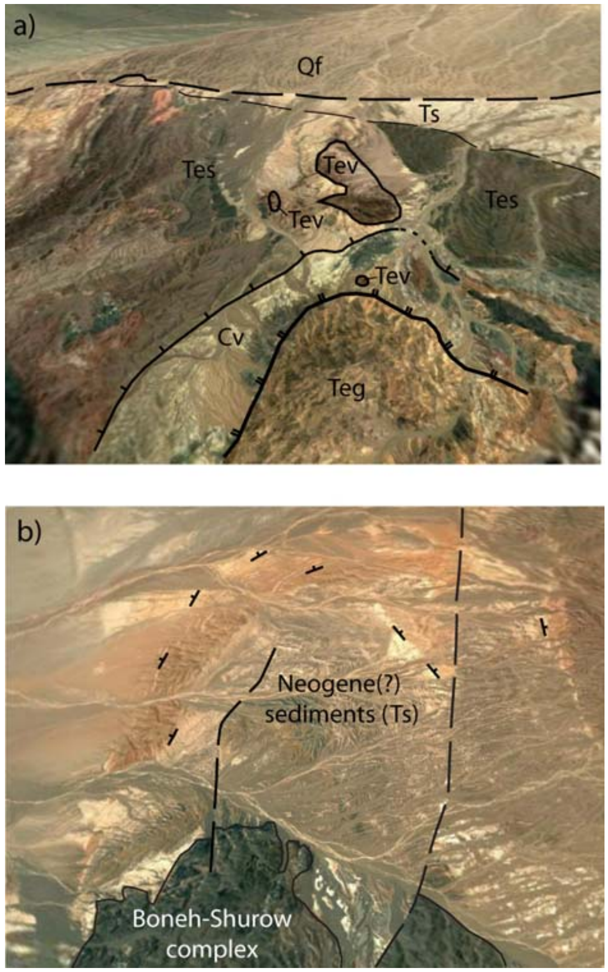

Figure 4. Oblique high-resolution satellite images. a) View northeast along the eastern edge of Khoshoumi Mountain showing ESE dipping Eocene supradetachment basin deposits (Tes) intruded by Eocene hypabyssal rocks (Tev), faulted over CVSU (Cv) and Eocene gneiss (Teg). The Eocene sediments and volcanics are unconformably overlain by Neogene(?) sediments (Ts) and alluvial fan deposits (Qf). See Figure 3 for geologic map of this area. Width of view at center of image is 4.5 km. b) View west of the western margin of Boneh-Shurow Mountain showing broad, ~EW trending fold and opposing dips of Neogene(?) sediments. Width of view at center of image is 4.6 km. Images from Google Earth, ©2006 Google™, ©2007 Europa Technologies, ©2007 Digital Globe, ©2007 TerraMetrics

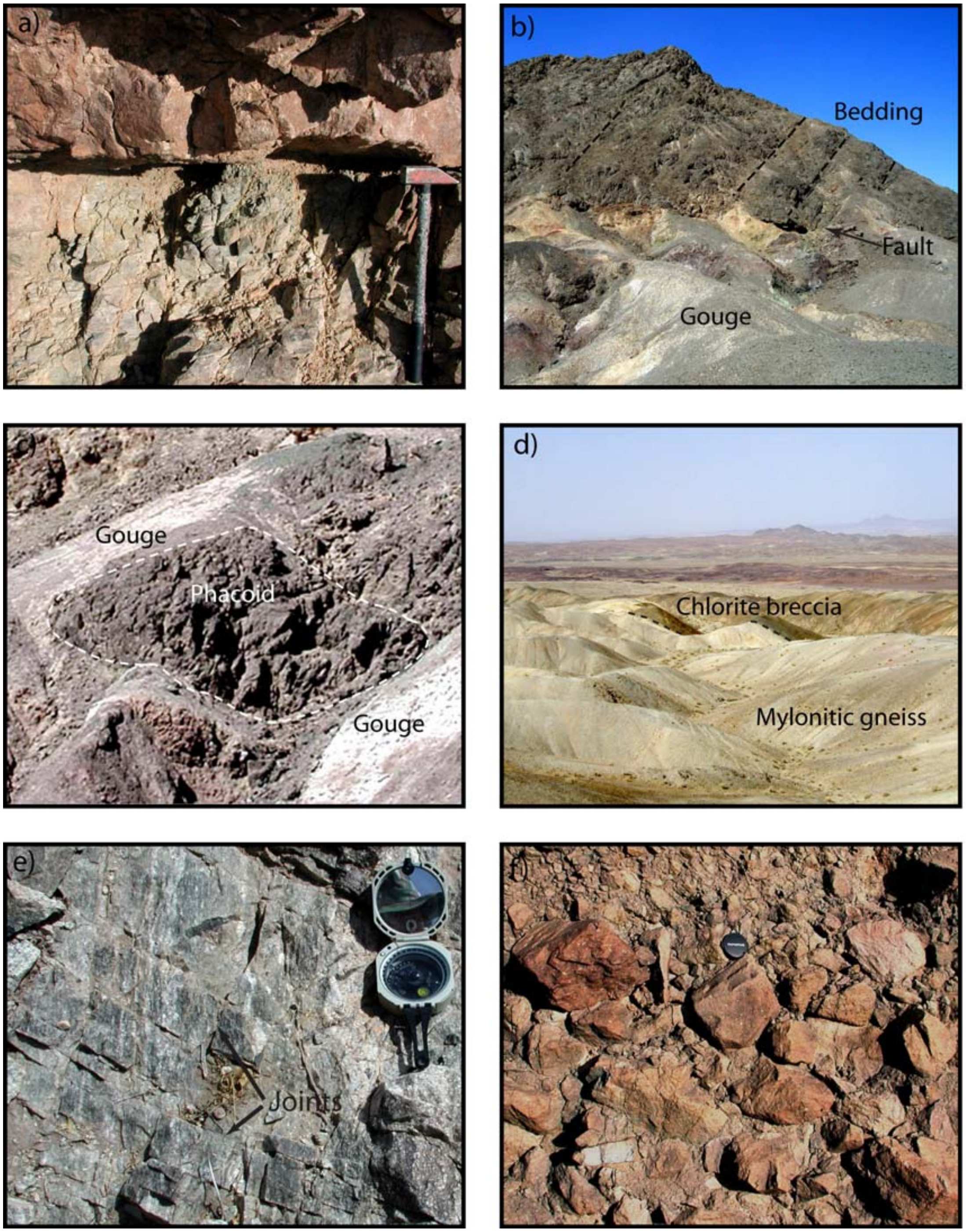
a)
b)
Bedding
Fault
Gouge
c)
Gouge
Phacoid
Gouge
d)
Chlorite breccia
Mylonitic gneiss
e)
Joints

Figure 5. Field photographs of extensional features in the Saghand area. a) View NNE of detachment fault emplacing Cambrian volcanic strata over chlorite breccia of mylonitic Chapedony gneiss, Khoshoumi Mountain (locality of fault plane attitude, Figure 3). b) View north of steeply west tilted Cretaceous limestone faulted over cataclastic Cambrian shale and volcanics exhibiting chaos structure. Width of view is ~200 m. c) Close-up view of chaos structure showing phacoid (~3 m wide) surrounded by gouge. d) View west showing base of chlorite breccia zone (dark band in middle ground), west side of Kalut-e-Chapedony. Light-grey rocks in the foreground are mylonitic gneiss of the Chapedony complex. Width of view in foreground is ~200 m. e) S70W lineation in mylonitic Chapedony gneiss, with foliation-normal conjugate joints, west side of Kalut-e-Chapedony. Width of view is 42 cm. f) Monolithic scarp breccia of Cambrian volcanic rocks in Tertiary supradetachment basin, Khoshoumi Mountain. Width of view is 0.7 m.

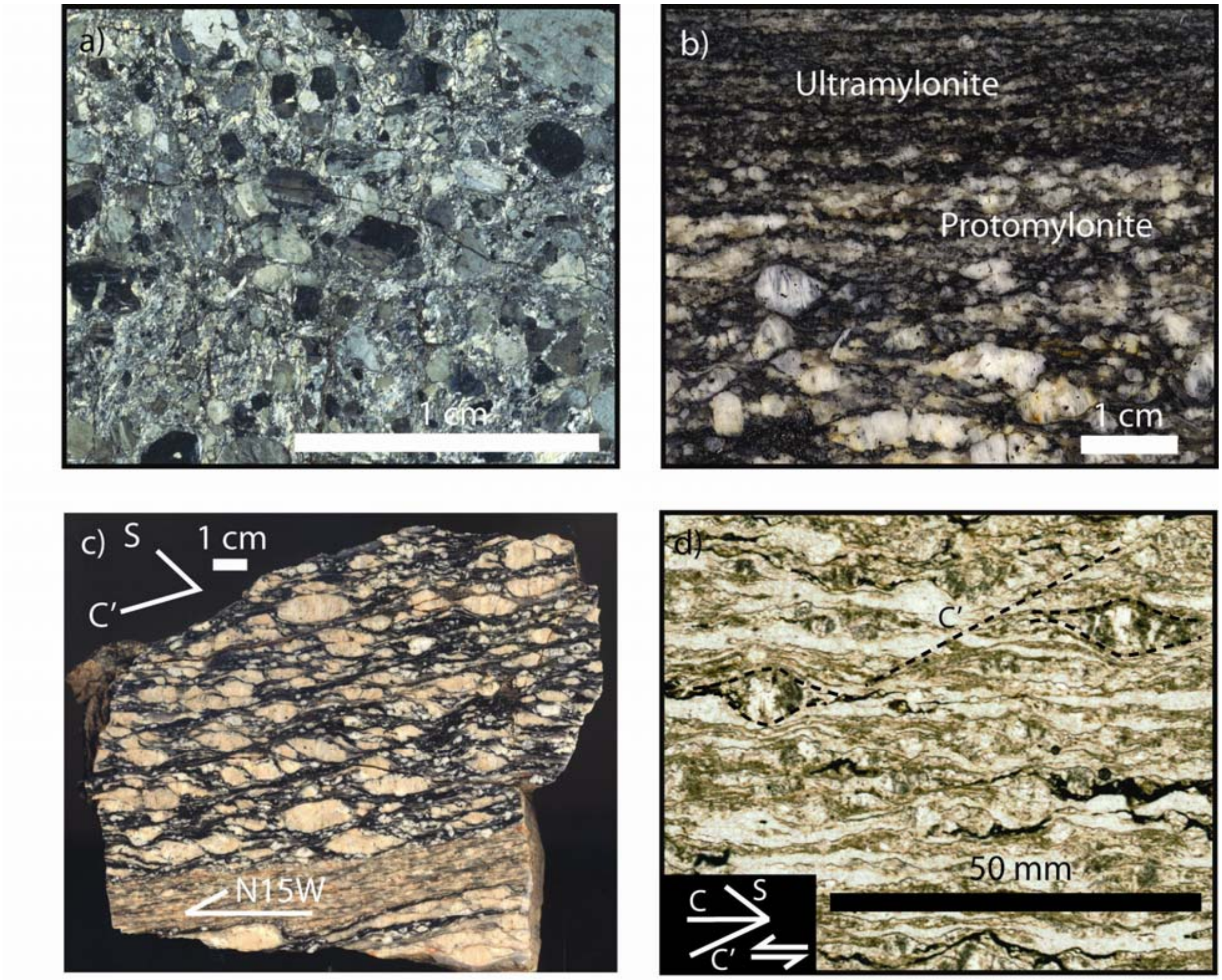

Figure 6. Photomicrographs/hand sample photos of fault- and shear zone-related rocks in the area. a) Photomicrograph of chlorite breccia from Neybaz Mountain. b) Polished slab of mylonitic Chapedony gneiss showing abrupt transition from ultramylonite to protomylonite, Kalut-e-Chapedony. c) Polished slab of S-C mylonite with top to the N15W shear sense, Neybaz Mountain. d) Photomicrograph of mylonitic gneiss showing sigmoid porphyroclasts and extensional shear bands indicating top to the left shear sense, Kalut-e-Chapedony.

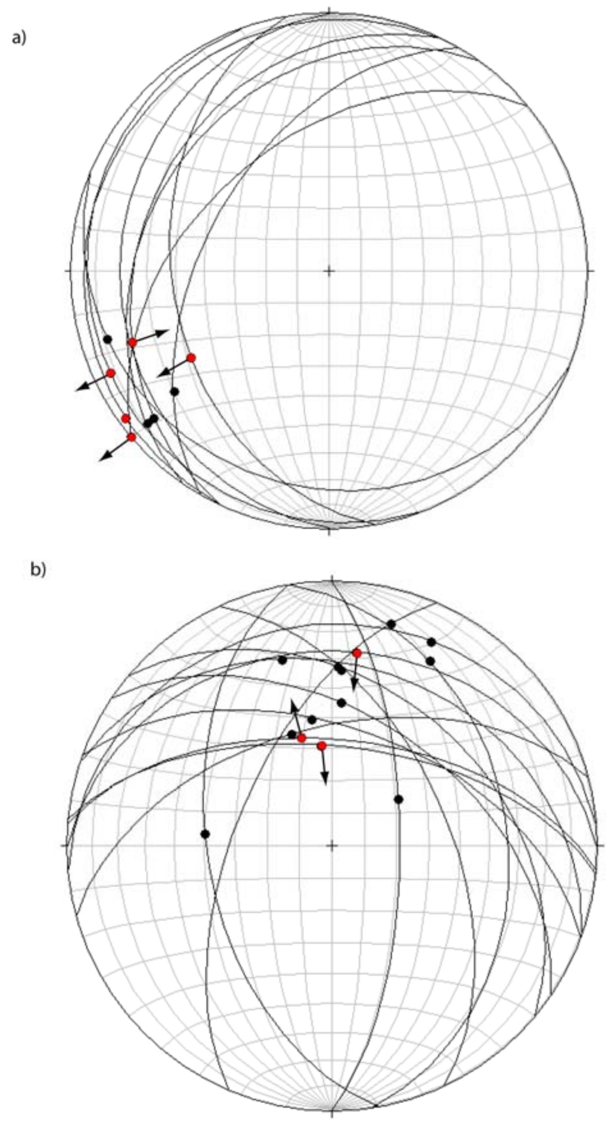

Figure 7. Lower-hemisphere equal-area plots of mylonitic foliation and lineation orientations from a) Kalut-e-Chapedony and b) Khoushoumi Mountain. Red dots indicate oriented samples from which sense-of-shear directions were determined, arrows indicate relative motion of the top with respect to the bottom.

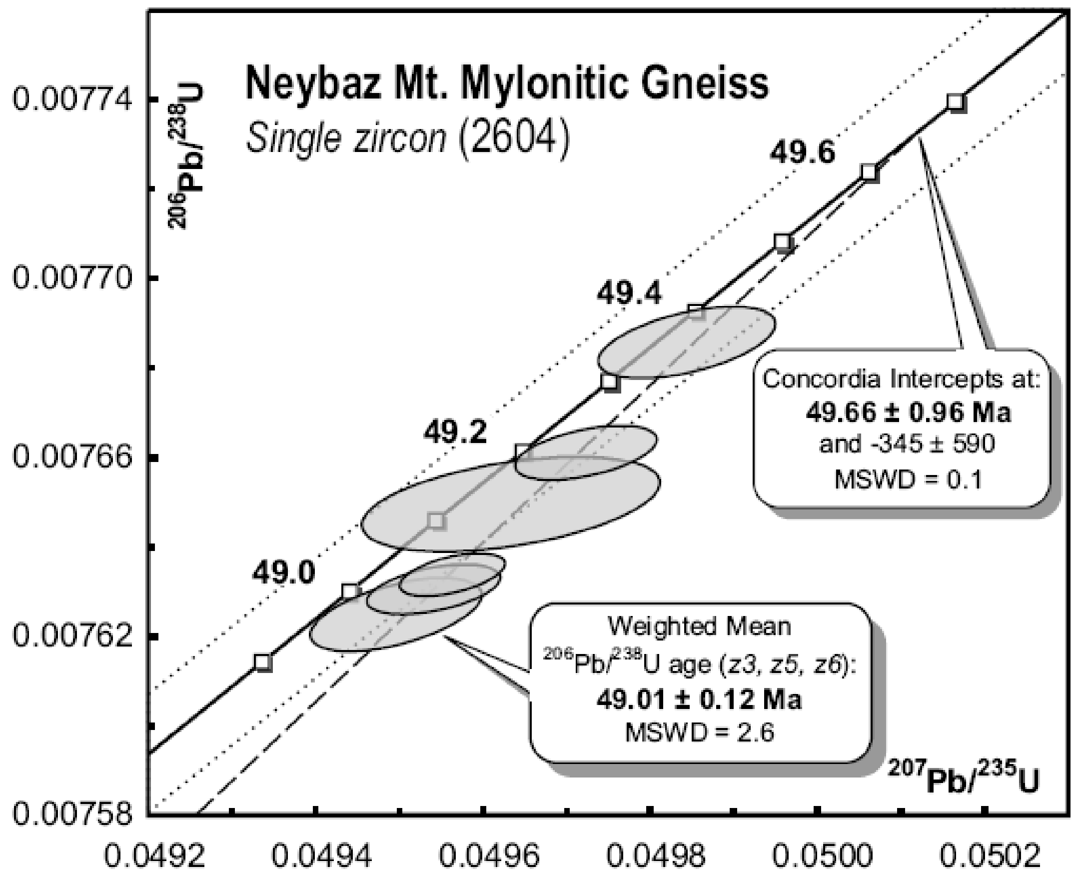

Figure 8. Concordia plot for zircons from sample 2604, a mylonitic gneiss from the southern edge of Neybaz Mountain (see Figure 6c).

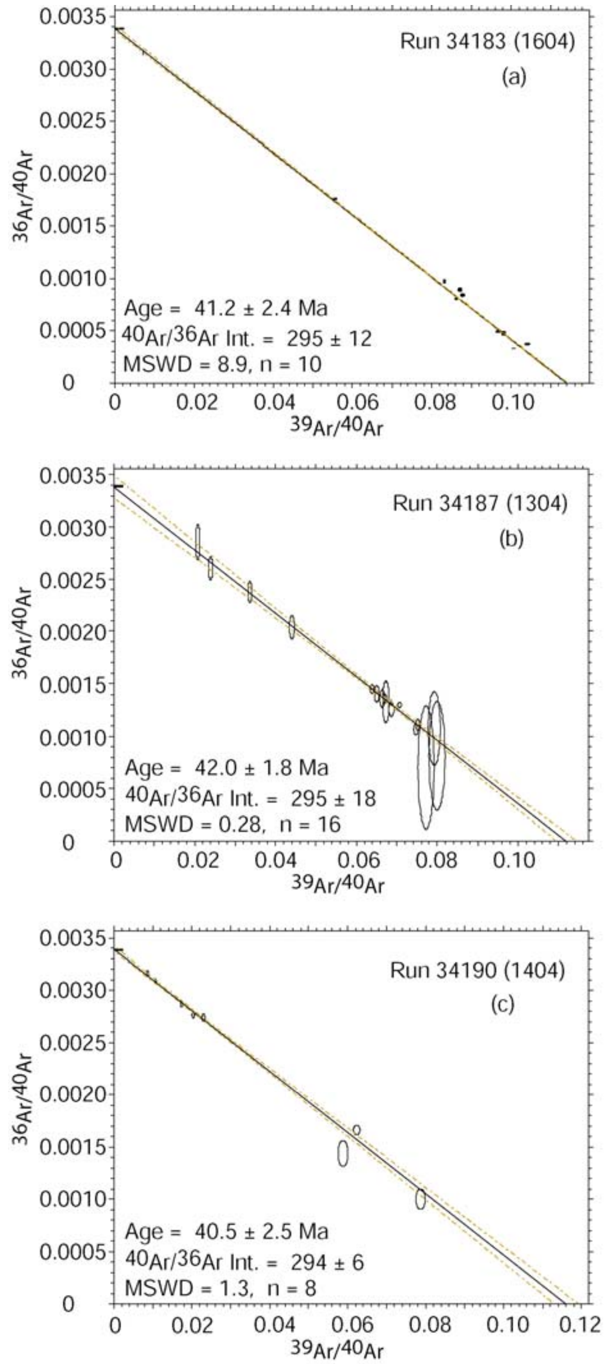

Figure 9. ^{40}Ar/^{39}Ar inverse isochron diagrams. All uncertainties are given at 95% confidence level. a) 1604 biotite single grain total fusion analyses. The isochron exhibits excess scatter and the age uncertainty is expanded by *t**sqrt(MSWD). b) 1304 plagioclase step-heating of two multi-grain aliquots. c) 1404 alkali feldspar single grain total fusion analyses.

a)

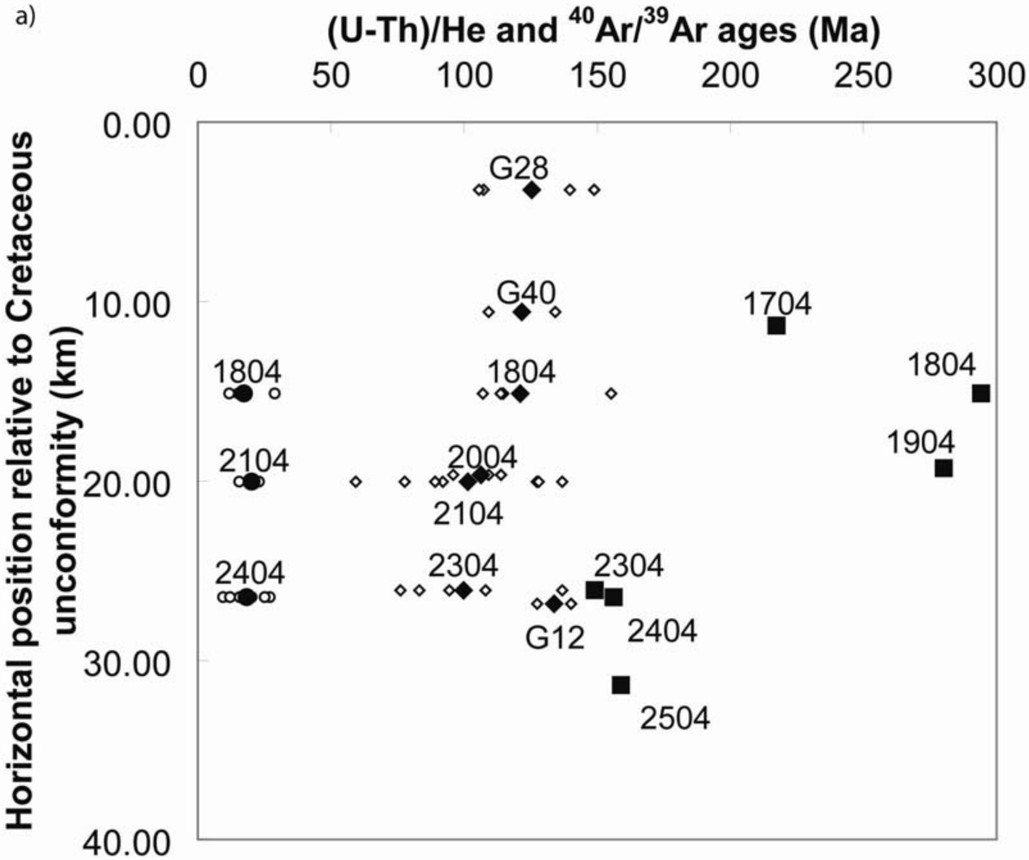
(U-Th)/He and ^{40}Ar/^{39}Ar ages (Ma)
0
50
100
150
200
250
300
Horizontal position relative to Cretaceous unconformity (km)
0.00
10.00
20.00
30.00
40.00
G28
G40
1704
1804
1804
1804
2104
2004
2104
1904
2404
2304
2304
G12
2404
2504

b)

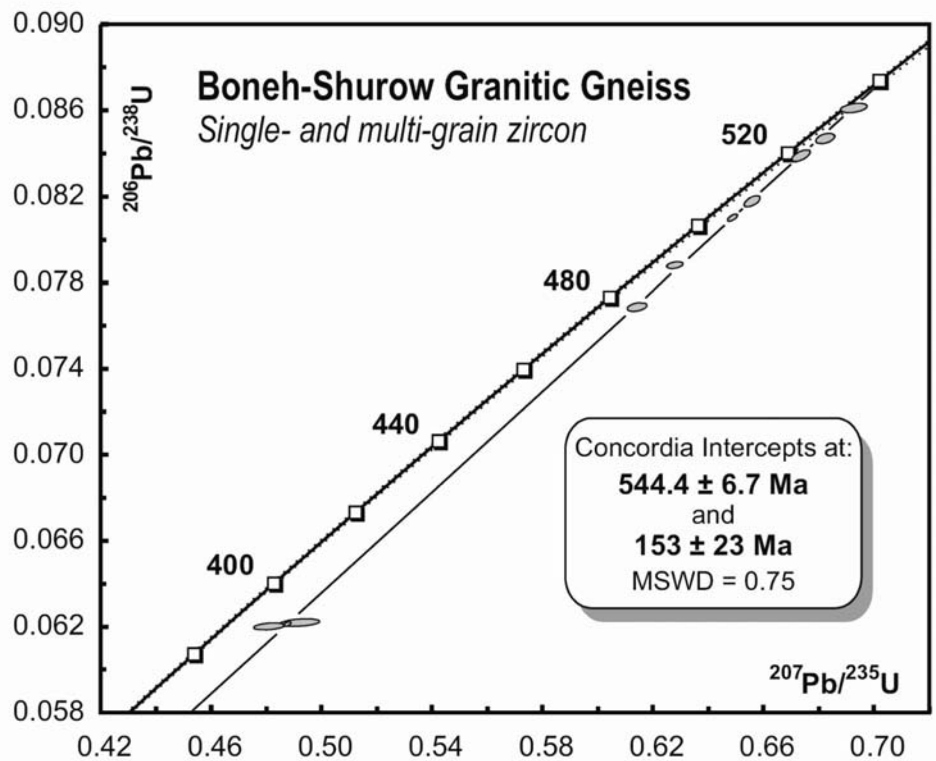
Boneh-Shurow Granitic Gneiss
Single- and multi-grain zircon
^{206}Pb/^{238}U
^{207}Pb/^{235}U
520
480
440
400
Concordia Intercepts at:
544.4 ± 6.7 Ma
and
153 ± 23 Ma
MSWD = 0.75
0.090
0.086
0.082
0.078
0.074
0.070
0.066
0.062
0.058
0.42
0.46
0.50
0.54
0.58
0.62
0.66
0.70

Figure 10. Thermochronologic data from the eastern domain. a) (U-Th)/He apatite (circles) and zircon (diamonds) ages, along with $^{40}Ar/^{39}Ar$ biotite ages (squares) from eastern domain samples, plotted as a function of horizontal position within the east-tilted crustal section. For (U-Th)/He data, individual replicates are shown with open symbols, and mean ages are shown with filled symbols. Sample positions were determined by projection onto the direction N60W. b) U-Pb concordia diagram for zircons from the Boneh-Shurow complex (see Ramezani and Tucker (2003) for analytical details). The upper intercept age is interpreted as the crystallization age of the protoliths, while the lower intercept age may reflect Pb loss resulting from rapid uplift.

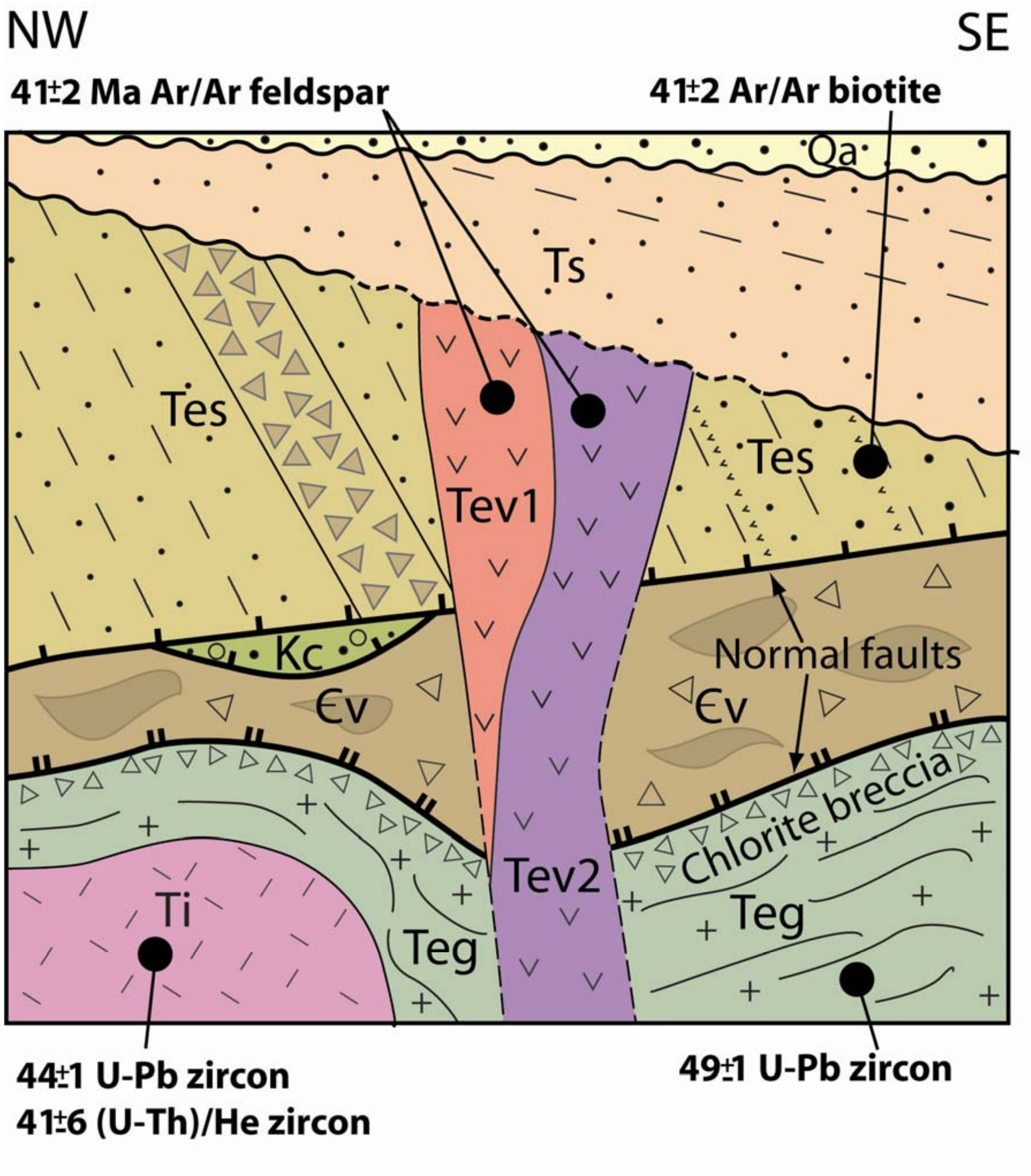

Figure 11. Summary of superposition relationships and $^{40}Ar/^{39}Ar$ data for the Khoshoumi Mountain area (Figures 2 and 3). Solid lines indicate mapped relationships, and dashed lines indicate inferred relationships discussed in text.

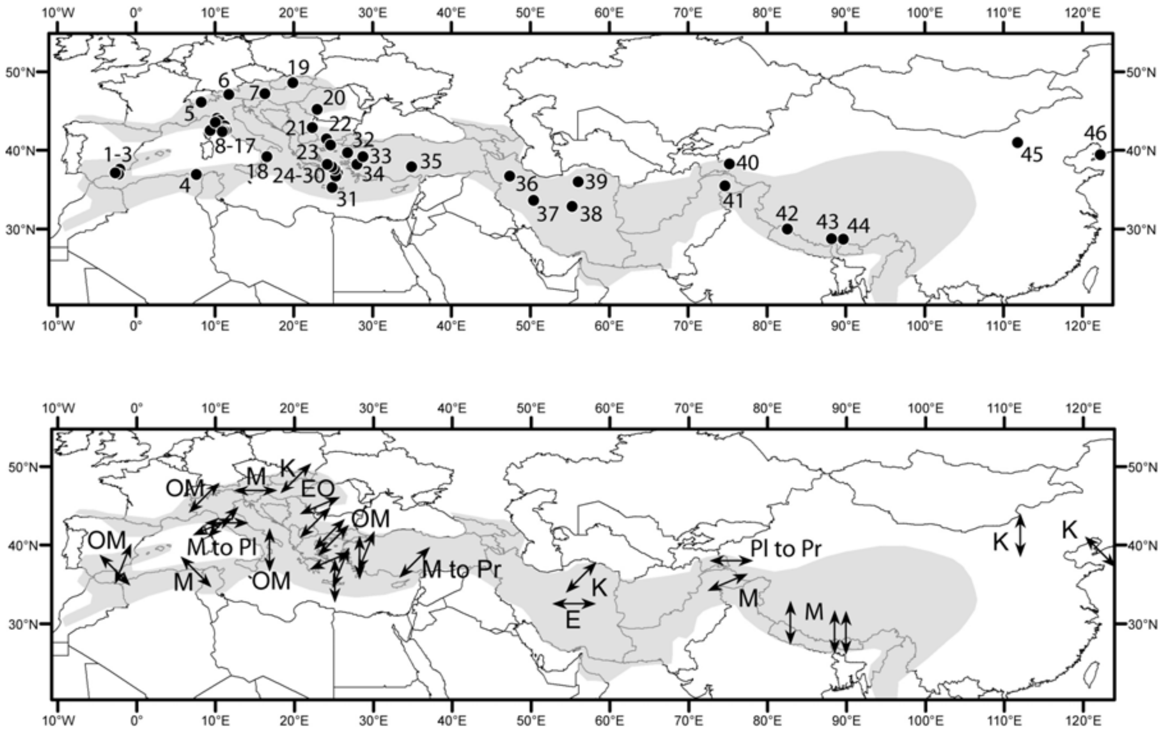

Figure 12. Map of Cretaceous to Tertiary metamorphic core complexes along the Alpine-Himalaya orogen, showing context of Iranian examples. (a) Locations of core complexes, (b) Extension directions and ages of selected core complexes. Shaded area is the approximate limit of the Tethysides, modified from Sengor (1987). Abbreviations: K=Cretaceous, E=Eocene, O=Oligocene, M=Miocene, Pl=Pliocene, Pr=Present. References in Table 1.

TABLE S1. U-Pb DATA

Sample Fract'ns†	Pb_c‡ (pg)	Pb^*/Pb_c‡	Th/U	$^{206}Pb/^{204}Pb$§	$^{208}Pb/^{206}Pb$#	Ratios $^{206}Pb/^{238}U$††	error (2σ%)	$^{207}Pb/^{235}U$††	error (2σ%)	$^{207}Pb/^{206}Pb$††	error (2σ%)	Age (Ma) $^{206}Pb/^{238}U$	$^{207}Pb/^{235}U$	$^{207}Pb/^{206}Pb$	corr. coef.
Mylonitic gneiss – Neybaz Mountain (2604)															
32° 29.952' N, 55° 6.343' E															
z2	0.7	48	0.52	2944.4	0.166	0.007686	(.09)	0.04984	(.17)	0.04704	(.15)	**49.35**	**49.39**	**51.1**	0.521
z4	0.3	63	0.52	3848.4	0.166	0.007661	(.06)	0.04972	(.14)	0.04707	(.12)	**49.20**	**49.27**	**53.0**	0.494
z1	0.6	34	0.40	2137.8	0.128	0.007650	(.11)	0.04963	(.29)	0.04706	(.26)	**49.12**	**49.19**	**52.3**	0.451
z3	0.7	96	0.37	6080.9	0.120	0.007630	(.06)	0.04954	(.13)	0.04709	(.12)	**49.00**	**49.10**	**53.8**	0.477
z5	0.7	41	0.53	2509.4	0.170	0.007625	(.09)	0.04950	(.17)	0.04708	(.14)	**48.97**	**49.06**	**53.3**	0.551
z6	0.3	107	0.52	6489.2	0.166	0.007634	(.05)	0.04957	(.10)	0.04709	(.09)	**49.02**	**49.12**	**53.9**	0.517

† All analyses are annealed and chemically treated single zircon grains.
‡ Pb_c is total common Pb in analysis. Pb* is radiogenic Pb concentration.
§ Measured ratio corrected for spike and fractionation only.
# Radiogenic Pb ratio.
†† Corrected for fractionation, spike, blank, and initial common Pb. Mass fractionation correction of 0.25%/amu ± 0.04%/amu (atomic mass unit) was applied to single-collector Daly analyses. Total procedural blank was less than 0.7 pg for Pb and less than 0.1 pg for U. Blank isotopic composition: 206Pb/204Pb = 18.27 ± 0.1, 207Pb/204Pb =15.59 ± 0.1, 208Pb/204Pb = 38.12 ± 0.1.
Corr. coef. = correlation coefficient.
Age calculations are based on the decay constants of Steiger and Jäger (1977).

TABLE S2. $^{40}Ar/^{39}Ar$ data for western domain samples

Sample Run ID	Power (W)	^{40}Ar (nA)	σ (nA)	^{39}Ar (nA)	σ (nA)	^{38}Ar (nA)	σ (nA)	^{37}Ar (nA)	σ (nA)	^{36}Ar (nA)	σ (nA)	$^{40}Ar^*/^{39}Ar_K$	σ	$\%^{40}Ar^*$	Age (Ma)	σ Ma
Sample 1604, biotite																
32° 25.849' N, 55° 9.516' E																
34183-01	5	1.00664	0.00102	0.08679	0.00022	0.00128	0.00002	0.00440	0.00005	0.00081	0.00001	8.8459	0.0603	76.27	41.56	0.28
34183-02	5	1.48920	0.00096	0.14991	0.00038	0.00207	0.00003	0.00152	0.00005	0.00048	0.00001	8.9835	0.0412	90.44	42.20	0.19
34183-03	5	12.12987	0.00531	0.08692	0.00022	0.00849	0.00004	0.00149	0.00004	0.03813	0.00005	9.9132	1.0836	7.10	46.51	5.02
34183-04	5	0.92257	0.00133	0.05141	0.00017	0.00098	0.00002	0.00253	0.00005	0.00162	0.00001	8.6378	0.1218	48.13	40.59	0.57
34183-05	5	0.36978	0.00053	0.03632	0.00013	0.00054	0.00002	0.00149	0.00005	0.00018	0.00001	8.7524	0.0827	85.96	41.13	0.38
34183-06	5	1.31457	0.00143	0.12734	0.00026	0.00179	0.00002	0.00437	0.00007	0.00065	0.00002	8.8185	0.0552	85.42	41.43	0.26
34183-07	5	0.68070	0.00090	0.07099	0.00022	0.00099	0.00002	0.00106	0.00004	0.00025	0.00001	8.5315	0.0520	88.98	40.10	0.24
34183-08	5	0.68510	0.00100	0.05976	0.00015	0.00101	0.00002	0.00124	0.00004	0.00061	0.00002	8.4544	0.0928	73.75	39.74	0.43
34183-09	5	0.65149	0.00113	0.05718	0.00021	0.00086	0.00002	0.00295	0.00005	0.00055	0.00001	8.5656	0.0739	75.19	40.26	0.34
34183-10	5	0.77398	0.00104	0.06435	0.00012	0.00103	0.00002	0.00221	0.00005	0.00075	0.00002	8.6000	0.0989	71.51	40.42	0.46
Sample 1304, plagioclase																
32° 26.779' N, 55° 9.707' E																
34187-01B	0.6	0.30214	0.00132	0.01339	0.00013	0.00031	0.00004	0.06957	0.00039	0.00063	0.00003	9.0081	0.7937	39.77	42.31	3.68
34187-01C	0.9	0.44673	0.00129	0.02925	0.00013	0.00049	0.00004	0.21280	0.00073	0.00068	0.00003	8.9763	0.3534	58.49	42.17	1.64
34187-01D	1.2	0.66043	0.00202	0.04975	0.00018	0.00077	0.00004	0.39962	0.00139	0.00081	0.00003	9.1415	0.2127	68.48	42.93	0.99
34187-01E	1.7	0.65136	0.00164	0.04940	0.00018	0.00076	0.00004	0.45224	0.00159	0.00084	0.00003	8.9209	0.2129	67.23	41.91	0.99
34187-01F	2.2	0.09436	0.00079	0.00757	0.00010	0.00015	0.00004	0.09685	0.00074	0.00013	0.00003	8.5925	1.3303	68.29	40.38	6.18
34187-01G	2.7	0.05402	0.00083	0.00421	0.00008	0.00008	0.00003	0.05682	0.00052	0.00005	0.00003	10.2622	2.2736	79.33	48.13	10.52
34187-01H	3.2	0.06241	0.00079	0.00504	0.00009	0.00008	0.00003	0.06581	0.00053	0.00007	0.00003	9.5098	1.9512	76.14	44.64	9.05

TABLE S2, continued. $^{40}Ar/^{39}Ar$ data for western domain samples

Sample Run ID	Power (W)	^{40}Ar (nA)	σ (nA)	^{39}Ar (nA)	σ (nA)	^{38}Ar (nA)	σ (nA)	^{37}Ar (nA)	σ (nA)	^{36}Ar (nA)	σ (nA)	$^{40}Ar^{*}/^{39}Ar_{K}$	σ	$\%^{40}Ar^{*}$	Age (Ma)	σ Ma
Sample 1304, plagioclase																
32° 26.779' N, 55° 9.707' E																
34187-02B	0.4	0.17395	0.00076	0.00364	0.00007	0.00012	0.00003	0.00995	0.00020	0.00050	0.00003	7.5722	2.5565	15.81	35.64	11.91
34187-02C	0.6	0.29381	0.00094	0.00998	0.00009	0.00023	0.00003	0.04958	0.00032	0.00071	0.00003	8.8459	0.9521	29.94	41.56	4.42
34187-02D	0.9	0.36705	0.00110	0.02455	0.00012	0.00035	0.00003	0.17074	0.00075	0.00054	0.00003	8.9863	0.3875	59.83	42.21	1.80
34187-02E	1.2	0.70299	0.00192	0.04745	0.00020	0.00087	0.00004	0.34992	0.00110	0.00105	0.00003	8.9026	0.2173	59.78	41.82	1.01
34187-02F	1.5	0.90571	0.00211	0.06439	0.00024	0.00111	0.00004	0.52063	0.00140	0.00131	0.00003	8.7347	0.1671	61.75	41.04	0.78
34187-02G	1.8	0.73461	0.00173	0.04732	0.00020	0.00090	0.00004	0.42391	0.00111	0.00117	0.00003	8.9623	0.2202	57.38	42.10	1.02
34187-02H	2.2	0.43084	0.00116	0.02987	0.00017	0.00052	0.00004	0.32917	0.00083	0.00063	0.00003	9.1683	0.3291	63.08	43.06	1.53
34187-02I	3.5	0.15289	0.00081	0.01039	0.00009	0.00016	0.00003	0.13484	0.00087	0.00024	0.00003	9.0646	0.9086	61.03	42.58	4.22
34187-02J	7	0.29046	0.00093	0.00707	0.00009	0.00024	0.00003	0.08577	0.00046	0.00078	0.00003	9.5838	1.3943	23.13	44.98	6.46
Sample 1404, alkali feldspar																
32° 26.599' N, 55° 9.830' E																
34190-02	4	0.35877	0.00059	0.00388	0.00003	0.00029	0.00001	0.00308	0.00009	0.00111	0.00001	8.2742	1.0551	8.93	38.90	4.91
34190-03	4	0.12340	0.00044	0.00774	0.00007	0.00015	0.00001	0.03317	0.00024	0.00021	0.00001	8.1706	0.2620	51.08	38.42	1.22
34190-04	4	0.04751	0.00036	0.00284	0.00004	0.00006	0.00001	0.05492	0.00023	0.00008	0.00001	9.7939	0.6852	57.79	45.96	3.17
34190-05	4	0.60345	0.00067	0.00530	0.00004	0.00045	0.00001	0.00341	0.00008	0.00191	0.00001	7.4245	1.0795	6.52	34.95	5.03
34190-06	4	0.48638	0.00093	0.01001	0.00008	0.00041	0.00001	0.01475	0.00012	0.00135	0.00001	8.8744	0.4743	18.25	41.69	2.20
34190-07	4	0.33082	0.00076	0.00773	0.00007	0.00026	0.00001	0.09542	0.00034	0.00093	0.00001	8.2171	0.4738	19.02	38.64	2.20
34190-10	4	0.42792	0.00059	0.00744	0.00007	0.00040	0.00001	0.00309	0.00009	0.00123	0.00001	8.7855	0.6084	15.27	41.28	2.83
34190-11	4	0.05779	0.00033	0.00461	0.00005	0.00009	0.00001	0.07763	0.00030	0.00008	0.00001	8.9412	0.4044	70.52	42.00	1.88

TABLE S3. ^{40}Ar/^{39}Ar data for eastern domain samples

Sample 1704, biotite, 1.50 mg, J = 0.00151862 ± 0.0952%
32° 30.712' N, 55° 33.490 E

Step	T (C)	t (min.)	36Ar	37Ar	38Ar	39Ar	40Ar	%40Ar*	% 39Ar released	Ca/K	40Ar*/39ArK	Age (Ma)	1 s.d.
1	650	12	1.185	0.489	0.234	0.123	355.438	5.2	0.1	14.559186	159.044460	390.30	63.44
2	725	12	1.174	0.142	0.236	0.933	377.176	12.3	0.6	0.55502762	47.501559	125.66	5.75
3	790	12	6.450	0.583	1.280	6.770	2330.42	21.5	4.4	0.31401927	74.009831	192.16	2.14
4	850	12	5.760	0.484	1.429	25.468	3750.04	56.6	16.7	0.06929389	83.637632	215.72	1.02
5	905	12	0.666	0.286	0.367	18.285	1695.17	90.0	12.0	0.05703138	76.650557	198.65	0.67
6	960	12	0.676	0.363	0.364	19.795	1802.18	90.6	12.9	0.06686444	82.111305	212.00	0.71
7	1015	12	0.692	0.592	0.458	25.864	2329.33	92.6	16.9	0.08345883	83.238422	214.75	0.67
8	1055	12	0.566	7.725	0.548	32.568	3071.00	95.6	21.3	0.86507904	90.257038	231.74	0.75
9	1095	12	0.435	11.578	0.260	13.478	1237.73	92.0	8.8	3.13511068	83.669016	215.79	0.69
10	1135	12	0.228	2.297	0.092	4.805	421.639	89.9	3.1	1.74393691	73.373017	190.59	0.65
11	1180	12	0.289	2.719	0.109	2.372	254.683	74.1	1.6	4.18481533	70.228433	182.82	0.71
12	1250	12	0.272	3.454	0.089	0.979	151.366	55.9	0.6	12.9139448	68.771262	179.21	1.50
13	1400	12	0.527	8.581	0.116	1.436	621.574	78.8	0.9	21.9318247	327.440483	728.19	3.44
								Cumulative %39Ar released =	100.0		Total gas age =	218.27	0.51

Sample 1804, biotite, 0.80 mg, J = 0.00149439 ± 0.1458%
32 30.554' N, 55 31.001' E

Step	T (C)	t (min.)	36Ar	37Ar	38Ar	39Ar	40Ar	%40Ar*	% 39Ar released	Ca/K	40Ar*/39ArK	Age (Ma)	1 s.d.
1	650	12	1.796	0.074	0.343	0.046	522.880	2.2	0.1	5.95967947	318.279303	701.94	130.97
2	725	12	0.813	0.270	0.187	0.235	253.190	9.7	0.6	4.25424452	99.455224	249.98	15.85
3	790	12	2.886	1.506	0.553	1.425	929.788	12.1	3.9	3.91284014	78.089842	199.13	6.23
4	840	12	11.986	2.349	2.338	4.194	3852.95	11.6	11.5	2.07250874	107.299564	268.30	5.57
5	890	12	0.657	0.462	0.175	3.853	630.711	73.4	10.5	0.44347792	116.639294	289.87	1.33
6	940	12	0.473	1.198	0.178	7.582	1024.44	89.1	20.7	0.58441382	118.678318	294.55	1.10
7	990	12	0.382	4.314	0.165	8.278	1093.15	92.3	22.6	1.92831363	120.332481	298.33	1.03
8	1040	12	0.362	8.471	0.126	5.903	857.919	90.8	16.1	5.31528882	129.773723	319.78	1.13
9	1100	12	0.284	6.263	0.080	3.317	501.455	88.6	9.1	6.9971508	129.026930	318.09	2.15
10	1180	12	0.157	3.610	0.034	0.727	144.996	83.2	2.0	18.4650128	131.332632	323.29	5.00
11	1400	12	0.593	9.159	0.134	1.005	314.117	44.8	2.7	34.046981	122.095747	302.36	3.17
								Cumulative %39Ar released =	100.0		Total gas age =	295.36	1.08

TABLE S3, continued. $^{40}Ar/^{39}Ar$ data for eastern domain samples

Sample 1904, biotite, 1.40 mg, J = 0.00151068 ± 0.0997%
32° 31.949' N, 55° 28.705' E

Step	T (C)	t (min.)	36Ar	37Ar	38Ar	39Ar	40Ar	%40Ar*	% 39Ar released	Ca/K	40Ar*/39ArK	Age (Ma)	1 s.d.
1	670	12	2.619	0.074	0.505	0.085	760.456	2.0	0.3	3.29046746	199.846312	475.97	76.49
2	750	12	1.167	1.361	0.272	2.426	400.266	18.3	8.5	2.11962627	28.717012	76.62	1.71
3	810	12	8.146	0.950	1.618	3.833	2590.26	10.7	13.4	0.9360999	72.270577	186.94	4.28
4	860	12	1.858	0.754	0.368	2.841	836.066	38.0	10.0	1.00241183	109.783520	276.83	2.03
5	910	12	0.284	1.139	0.118	3.425	541.73	89.3	12.0	1.25615248	136.359062	337.91	1.52
6	960	12	0.336	3.017	0.119	3.520	617.767	88.2	12.4	3.23944637	150.548182	369.70	1.69
7	1010	12	0.400	8.050	0.256	5.937	843.91	89.4	20.8	5.12759068	124.761893	311.51	1.14
8	1060	12	0.248	6.288	0.123	3.689	533.269	91.3	12.9	6.44852923	127.512595	317.81	1.56
9	1120	12	0.199	6.095	0.131	1.914	292.433	88.3	6.7	12.0675928	121.608253	304.27	1.72
10	1190	12	0.152	2.269	0.029	0.465	113.326	77.9	1.6	18.5272295	139.225482	344.38	9.22
11	1400	12	0.564	1.633	0.115	0.360	215.684	13.0	1.3	17.2163975	70.060261	181.50	10.22
								Cumulative %39Ar released =	100.0		Total gas age =	281.32	1.17

Sample 2304, biotite, 1.40 mg, J = 0.0053346 ± 0.1091%
32° 31.914' N, 55° 28.775' E

Step	T (C)	t (min.)	36Ar	37Ar	38Ar	39Ar	40Ar	%40Ar*	% 39Ar released	Ca/K	40Ar*/39ArK	Age (Ma)	1 s.d.
1	680	12	2.871	0.025	0.541	0.382	816.288	-0.1	0.2	0.2535515	-2.737221	-7.61	-16.88
2	760	12	3.065	0.212	0.655	7.524	1167.750	25.9	4.1	0.10915855	39.781554	107.12	1.06
3	810	12	9.132	0.373	2.014	22.983	3845.67	32.7	12.4	0.06287337	54.849739	146.09	1.08
4	855	12	3.572	0.314	1.071	29.818	2716.07	63.2	16.1	0.04079556	57.564565	153.02	0.65
5	900	12	0.632	0.223	0.564	33.838	2156.4	92.8	18.3	0.02553054	58.971072	156.61	0.50
6	945	12	1.104	0.626	1.057	62.222	3799.98	92.4	33.7	0.03897552	56.539535	150.41	0.48
7	990	12	0.339	0.362	0.265	15.118	968.434	92.5	8.2	0.09276471	58.218381	154.69	0.54
8	1035	12	0.195	0.298	0.109	5.923	404.808	92.1	3.2	0.19492001	59.550334	158.08	0.65
9	1085	12	0.117	0.775	0.066	3.081	217.681	96.0	1.7	0.97475115	60.499413	160.49	1.12
10	1150	12	0.107	0.689	0.043	1.641	128.919	95.0	0.9	1.62734494	55.533265	147.84	0.99
11	1400	12	0.376	1.726	0.092	2.271	242.653	57.0	1.2	2.94689669	45.989171	123.28	1.96
								Cumulative %39Ar released =	100.0		Total gas age =	149.75	0.46

TABLE S3, continued. $^{40}Ar/^{39}Ar$ data for eastern domain samples

Sample 2404, biotite, 1.40 mg, J = 0.0015473 ± 0.1123%
32° 32.028' N, 55° 24.747' E

Step	T (C)	t (min.)	36Ar	37Ar	38Ar	39Ar	40Ar	%40Ar*	% 39Ar released	Ca/K	40Ar*/39ArK	Age (Ma)	1 s.d.
1	690	12	3.406	0.024	0.639	0.635	991.380	2.2	0.3	0.32679748	35.408661	96.23	11.56
2	770	12	1.193	0.060	0.306	6.072	638.441	48.8	2.6	0.08543369	49.847487	134.04	0.92
3	810	12	6.691	0.108	1.513	18.082	2947.75	35.8	7.8	0.05163956	58.354398	155.95	1.07
4	850	12	2.619	0.144	0.983	33.458	2686.04	73.0	14.4	0.03721053	58.575993	156.52	0.60
5	890	12	0.164	0.041	0.332	23.681	1430.37	98.5	10.2	0.01496871	59.000941	157.61	0.52
6	930	12	0.393	0.089	0.928	64.871	3879.12	97.8	28.0	0.0118615	58.610905	156.61	0.48
7	970	12	0.241	0.024	0.317	22.562	1369.27	96.8	9.7	0.00919673	58.185798	155.52	0.55
8	1050	12	0.301	0.059	0.448	30.953	1918.05	96.8	13.3	0.01647972	59.750226	159.52	0.49
9	1140	12	0.141	0.051	0.375	26.447	1605.70	99.1	11.4	0.01667226	59.428109	158.70	0.48
10	1400	12	0.348	0.097	0.150	5.271	417.979	80.7	2.3	0.15911019	54.983769	147.30	0.69
								Cumulative %39Ar released =	100.0		Total gas age =	156.20	0.40
											Plateau age (steps 3-6) =	156.86	0.58

Sample 2504, biotite, 1.80 mg, J = 0.00152694 ± 0.0993%
32° 30.865' N, 55° 21.087' E

Step	T (C)	t (min.)	36Ar	37Ar	38Ar	39Ar	40Ar	%40Ar*	% 39Ar released	Ca/K	40Ar*/39ArK	Age (Ma)	1 s.d.
1	770	12	3.697	1.031	0.730	3.543	1178.11	10.6	4.8	1.21176812	37.252676	99.81	2.18
2	810	12	10.177	1.758	1.973	5.023	3212.25	9.8	6.8	1.45753771	63.094333	165.94	4.32
3	850	12	3.093	0.796	0.699	6.586	1255.83	30.1	8.9	0.50318861	57.018796	150.61	1.32
4	890	12	0.265	0.551	0.132	6.623	475.911	86.7	9.0	0.3463505	60.406719	159.17	0.52
5	930	12	0.341	1.193	0.237	11.971	818.517	90.7	16.2	0.41489475	60.692591	159.89	0.63
6	970	12	0.415	6.291	0.259	14.750	1004.91	90.4	20.0	1.7763699	60.653963	159.79	0.58
7	1050	12	0.565	30.581	0.310	15.826	1211.34	88.8	21.5	8.06318088	67.369872	176.65	0.63
8	1140	12	0.310	21.154	0.152	6.708	586.271	89.0	9.1	13.1792775	75.506441	196.86	0.72
9	1400	12	0.540	8.639	0.138	2.641	367.089	66.8	3.6	13.6726099	82.230342	213.39	1.84
								Cumulative %39Ar released =	100.0		Total gas age =	165.38	0.53
											Pseudo plateau age (steps 4-6) =	159.57	0.65

TABLE S4. (U-Th)/He analytical data for western domain samples

Apatite (U-Th)/He data, western domain							
Sample	No. of grains	U (ppm)	Th (ppm)	He (nmol/g)	F_T	Age (Ma) Raw	Age (Ma) Corrected
G30, Diorite, Daranjir Diorite							
32° 23.613' N, 55° 0.583' E							
	4	33	112	3.8	0.754	11.8	15.6
	1	45	122	5.3	0.678	13.2	19.4
	1	43	142	3.5	0.738	8.2	11.1
Mean							15.4
2σ							8.4
G27, Granite, Khoshoumi Granite							
32° 26.973' N, 55° 5.002' E							
	1	24	59	3.5	0.770	16.7	21.6
	1	26	59	4.1	0.780	18.7	23.9
Mean							22.8
2σ							3.3
0504, Non-mylonitic biotite gneiss, Chapedony complex							
32° 50.702' N, 55° 13.578' E							
	4	31	39	3.6	0.770	16.4	21.3
	2	27	28	2.4	0.778	13.2	17.0
	3	29	30	3.4	0.761	17.2	22.6
Mean							20.3
2σ							5.8

TABLE S4, continued. (U-Th)/He analytical data for western domain samples

Zircon (U-Th)/He data, western domain							
Sample	No. of grains	U (ppm)	Th (ppm)	He (nmol/g)	F_T	Age (Ma) Raw	Age (Ma) Corrected
G30, Diorite, Daranjir Diorite							
32° 23.613' N, 55° 0.583' E							
	1	872	1075	198	0.757	32.4	42.7
	1	504	667	104	0.774	28.8	37.2
	1	574	517	133	0.824	35.1	42.6
	1	240	322	56	0.816	32.6	39.9
Mean							40.6
2σ							5.2
G27, Granite, Khoshoumi Granite							
32° 26.973' N, 55° 5.002' E							
	1	862	237	169	0.768	33.8	43.9
	1	1128	251	187	0.783	29.0	36.9
	1	502	176	92	0.777	31.1	40.0
	1	594	165	112	0.791	32.6	41.2
Mean							40.5
2σ							5.8
0504, Non-mylonitic biotite gneiss, Chapedony complex							
32° 50.702' N, 55° 13.578' E							
	1	316	185	57	0.759	29.2	38.5
	1	241	269	49	0.785	29.2	37.2
	1	392	501	99	0.810	35.6	43.9
	1	343	322	71	0.784	31.1	39.7
	5	183	151	44	0.787	37.1	47.0
	1	208	124	43	0.781	33.5	42.9
	1	265	370	73	0.808	38.2	47.3
	1	290	399	77	0.777	36.9	47.5
	1	324	211	70	0.794	34.2	43.0
Mean							43.0
2σ							7.8
G18, Gneiss, Chapedony complex							
32° 50.039' N, 55° 18.538' E							
	1	962	472	249	0.848	42.5	50.1
	1	827	212	173	0.852	36.1	42.4
	1	597	167	178	0.865	51.3	59.3
	1	787	233	170	0.852	37.0	43.4
Mean							48.8
2σ							15.6

TABLE S5. (U-Th)/He analytical data for eastern domain samples

Apatite (U-Th)/He data, eastern domain							
Sample	No. of grains	U (ppm)	Th (ppm)	He (nmol/g)	F_T	Age (Ma) Raw	Age (Ma) Corrected
2404, Metapelitic schist, Boneh-Shurow complex							
32° 32.028' N, 55° 24.747' E							
	3	6	3	0.3	0.702	6.7	9.6
	4	7	5	0.5	0.661	12.2	18.4
	1	10	8	1.2	0.689	18.7	27.0
	1	5	3	0.4	0.739	11.7	15.8
	1	9	6	0.8	0.655	13.3	20.3
	1	6	5	0.3	0.735	8.9	12.1
	1	6	2	0.6	0.697	17.6	25.2
Mean							18.3
2σ							12.9
2104, Graywacke, Tashk Formation							
32° 31.917' N, 55° 28.776' E							
	4	31	33	2.4	0.731	11.4	15.6
	3	9	6	0.9	0.692	15.9	23.0
	4	11	11	1.0	0.705	13.8	19.5
	3	25	29	2.6	0.631	14.5	23.0
Mean							20.3
2σ							7.0
1804, Graywacke, Tashk Formation							
32° 30.554' N, 55° 31.001' E							
	2	11	7	1.4	0.726	21.0	29.0
	2	8	5	0.7	0.780	14.5	18.6
	1	18	9	1.3	0.788	12.1	15.4
	1	16	5	1.0	0.851	10.1	11.9
	1	16	13	0.9	0.756	8.9	11.8
Mean							17.3
2σ							14.2

TABLE S5, continued. (U-Th)/He analytical data for eastern domain samples

Zircon (U-Th)/He data, eastern domain							
Sample	No. of grains	U (ppm)	Th (ppm)	He (nmol/g)	F_T	Age (Ma) Raw	Age (Ma) Corrected
2304, Schist, Boneh-Shurow complex							
32° 31.914' N, 55° 28.775' E							
	1	283	144	94	0.710	54.2	76.1
	1	177	102	74	0.710	67.3	94.5
	1	637	360	307	0.716	77.6	108.1
	1	265	153	102	0.746	62.2	83.2
	4	348	195	221	0.744	102.2	136.8
Mean							99.7
2σ							48.0
G12, Quartz diorite, Boneh-Shurow complex							
32° 35.714' N, 55° 26.642' E							
	3	292	167	203	0.792	111.4	140.1
	4	452	274	284	0.783	100.1	127.5
Mean							133.8
2σ							17.9
2104, Graywacke, Tashk Formation							
32° 31.917' N, 55° 28.776' E							
	1	128	58	75	0.758	96.8	127.3
	1	146	47	83	0.745	95.8	128.1
	1	125	28	75	0.759	104.2	136.9
	1	308	99	106	0.753	58.7	77.7
	1	288	130	77	0.749	44.5	59.3
	5	231	83	93	0.738	68.0	92.0
	5	256	63	99	0.752	67.1	89.1
Mean							101.5
2σ							59.0
2004, Leucogranite							
32° 31.936' N, 55° 28.728' E							
	5	86	85	48	0.754	82.6	109.2
	5	96	99	58	0.774	88.3	113.9
	5	67	73	35	0.790	75.9	95.9
Mean							106.3
2σ							18.6

TABLE S5, continued. (U-Th)/He analytical data for eastern domain samples

Zircon (U-Th)/He data, eastern domain							
Sample	No. of grains	U (ppm)	Th (ppm)	He (nmol/g)	F_T	Age (Ma) Raw	Age (Ma) Corrected
1804, Graywacke, Tashk Formation							
32° 30.554' N, 55° 31.001' E							
	1	85	30	59	0.754	117.5	155.2
	1	171	91	102	0.796	96.9	121.5
	1	322	95	177	0.815	93.6	114.5
	1	279	146	154	0.776	89.4	114.8
	1	139	107	73	0.759	81.4	107.0
	5	212	95	110	0.751	85.7	113.7
Mean							121.1
2σ							34.7
G40, Tuffaceous rock, Tashk Formation							
32° 31.169' N, 55° 34.034' E							
	1	473	102	290	0.790	106.4	134.2
	1	425	338	223	0.739	80.9	109.2
Mean							121.7
2σ							35.3
G28, Rhyodacite, CVSU							
32° 27.465' N, 55° 36.338' E							
	1	148	108	115	0.806	120.3	148.9
	1	104	77	57	0.790	85.0	107.3
	1	105	67	77	0.831	116.3	139.7
	1	166	116	89	0.799	84.6	105.6
Mean							125.4
2σ							44.3

TABLE 1. Alpine-Himalayan metamorphic core complexes

Number (Fig. 12)	Location/Name	Age	Extension direction	Reference
	Spain			
1	Nevado-Filabrides	Late Oligocene-Late Miocene	NW-SE	Platt and Vissers, 1989
2	Sierra Alhamilla	Late Oligocene-Late Miocene	NNE-SSW	Platt and Vissers, 1989
3	Sierra de las Estancias	Late Oligocene-Early Miocene	NNE-SSW	Platzman and Platt, 2004
	Algeria			
4	Edough	Late Miocene	NW-SE	Caby et al., 2001
	Alps			
5	Simplon	Oligocene-Miocene	NE-SW	Mancktelow and Pavlis, 1994; Wawrzyniec et al., 2001
6	Brenner	Early Oligocene-Early Miocene	E-W	Axen et al., 1995; Wawrzyniec et al., 2001
7	Rechnitz	Miocene	E-W	Grassl et al., 2004; Ratschbacher et al., 1990
	Italy/Tyrrhenian Sea			
8	Corsica	Late Oligocene-Early Miocene	ENE-WSW	Brunet et al., 2000; Fournier et al., 1991
9	Alpi Apuane	Miocene	NE-SW	Carmignani and Roy, 1990; Carmignani et al, 1994
10	Monte Pisano	Pliocene	NE-SW	Brunet et al., 2000
11	Monticciano-Roccastrada	Pliocene	E-W	Brunet et al., 2000
12	Elba	Miocene	E-W	Brunet et al., 2000
13	Monte Romani	Miocene-Pliocene	ENE-WSW	Brunet et al., 2000
14	Uccellina	Miocene		Brunet et al., 2000
15	Monte Argentario	Miocene	ENE-WSW	Brunet et al., 2000
16	Gorgona	Miocene	NW-SE	Brunet et al., 2000
17	Giglio	Miocene	ENE-WSW	Jolivet et al., 1998
18	Calabrian	Middle Oligocene-Middle Miocene	N-S	Platt and Compagnani, 1990; Thomson, 1994; Wallis et al., 1993
	Carpathians			
19	Vepor	Cretaceous	NE-SW	Janak et al., 2001
20	Getic	Late Eocene-Oligocene	WSW-ENE	Fugenschuh and Schmid, 2005; Schmid et al., 1998
	Bulgaria/ Northern Greece			
21	Osogovo-Lisets	Middle Eocene-Early Oligocene	NE-SW	Kounov et al., 2004
22	Rhodope	Miocene	NE-SW	Dinter et al, 1995; van Hinsbergen and Meulenkamp, 2006
	Greece/Aegean Sea			
23	Thasos	Early-Middle Miocene	NE-SW	Wawrenitz and Krohe, 1998
24	Mykonos	Late Miocene	NE-SW	Lee and Lister, 1992
25	Naxos	Miocene	NNE-SSW	Lister et al., 1984
26	Ios	Miocene	NNE-SSW	Lister et al., 1984
27	Tinos	Miocene	NNE-SSW	Gautier and Brun, 1994; Ring et al., 2003
28	Andros	Miocene	NNE-SSW	Gautier and Brun, 1994
29	Evvia	Oligocene-Early Miocene	ENE-WSW	Gautier and Brun, 1994
30	Ikaria	Late Miocene-Pliocene	NNE-SSW	Kumerics et al., 2005
31	South Aegean (Cretan)	Early-Middle Miocene	N-S	Thomson et al., 1999; van Hinsbergen and Meulenkamp, 2006
	Turkey			
32	Kazdag	Late Oligocene	NNW-SSE	Okay and Satir, 2000
33	Simav	Early-Middle Miocene	NNE-SSW	Ring and Collins, 2005
34	Central Menderes	Miocene-Present	N-S	Gessner et al., 2001
35	Nigde	Miocene-Present	NE-SW	Whitney and Dilek, 1997
	Iran			
36	Takab-Zanjan	Miocene	NW-SE	Stockli et al., 2004
37	Golpaygan			Thiele et al., 1967; Tillman et al., 1981
38	Saghand	Middle Eocene	E-W	This paper
39	Biarjmand	Cretaceous	NE-SW	Hassanzadeh et al., 2005
	Himalaya			
40	Kongur Shan	Early Pliocene-Present	E-W	Brunel et al., 1994
41	Nanga Parbat	Early Miocene	WSW-ENE	Argles and Edwards, 2002; Hubbard et al., 1995
42	N. Himalayan gneiss domes	Miocene	N-S	Burchfiel et al., 1992; Yin et al., 1999
43	Mabja Dome	Miocene	N-S	Lee et al., 2004
44	Kangmar Dome	Miocene	N-S	Chen et al., 1990; Lee et al., 2000
	Eastern China			
45	Hohhot	Cretaceous	N-S	Davis et al., 2002
46	Liaonan	Early Cretaceous	NW-SE	Junlai et al., 2005

APPENDIX A. ANALYTICAL METHODS FOR U-Pb GEOCHRONOLOGY

Zircon was separated from bulk rock samples by standard crushing, heavy liquid, and magnetic separation techniques, and was subsequently handpicked using a binocular microscope, with selection based on clarity and crystal morphology. All grains were pre-treated to minimize the effects of Pb loss, by the method of thermal annealing and chemical leaching (chemical abrasion or CA-TIMS technique: Mattinson, 2005; Mundil et al., 2004) designed to preferentially remove the high-U parts of the zircon crystal that are most susceptible to Pb loss. Zircon grains are first annealed at 900°C for 60 hours and leached in 29M HF inside high-pressure Parr® vessels at 180°C for 12 hours. The partially dissolved sample is then fluxed successively with hot 4N HNO_3 and 6N HCl and thoroughly rinsed with ultra-pure water in between. Pre-treated and rinsed zircons were spiked with a mixed ^{205}Pb-^{233}U-^{235}U tracer solution and dissolved completely in 29M HF inside Parr® vessels at 220°C for 48-60 hours.

Dissolved Pb and U were chemically separated using a miniaturized HCl-based ion-exchange chromatography procedure modified after Krogh (1973), using 50 µl columns of AG1x8 anion-exchange resin. Both Pb and U were loaded with a silica gel - H_3PO_4 emitter solution (Gerstenberger and Haase, 1997) on single degassed Re filaments and their isotopic compositions were measured on the VG Sector 54 multi-collector thermal ionization mass spectrometer at MIT. Lead isotopic measurements were made in a peak-switching mode by ion counting using a Daly photomultiplier detector with a ^{206}Pb ion beam intensity of 0.5 to 2.0 x 10^{-13} Amps usually maintained in the course of data acquisition. Uranium isotopes were measured as oxide ions on three Faraday detectors in a static mode with an average $^{235}U^{16}O_2^+$ ion-beam intensity of 8.0 x 10^{-13} Amps.

Measured isotopic ratios were corrected for mass-dependent isotope fractionation in the mass spectrometer, as well as for U and Pb contributions from the spike, laboratory blanks and initial Pb in the sample. Details of fractionation and blank corrections are given in Table S1. The U-Pb data reduction, age calculation and error propagation follow the algorithm of Ludwig (1980) and the program ISOPLOT (Ludwig, 1991; version 3.14, 2004). All U-Pb dates are reported at 95% confidence levels.

Gerstenberger, H., and Haase, G., 1997, A highly effective emitter substance for mass spectrometric Pb isotope ratio determinations: Chemical Geology, v. 136, no. 3-4, p. 309-312.

Krogh, T.E., 1973, A low-contamination method for hydrothermal decomposition of zircon and extraction of U and Pb for isotopic age determinations: Geochimica et Cosmochimica Acta, v. 37, no. 3, p. 485-494.

Ludwig, K.R., 1980, Calculation of uncertainties of U-Pb isotope data: Earth and Planetary Science Letters, v. 46, no. 2, p. 212-220.

Ludwig, K.R., 1991, ISOPLOT; a plotting and regression program for radiogenic-isotope data; version 2.53: Open-File Report - U. S. Geological Survey, OF 91-0445.

Mattinson, J.M., 2005, Zircon U-Pb chemical abrasion (CA-TIMS) method; combined annealing and multi-step partial dissolution analysis for improved precision and accuracy of zircon ages: Chemical Geology, v. 220, no. 1-2, p. 47-66.

Mundil, R., Ludwig, K.R., Metcalfe, I., and Renne, P.R., 2004, Age and timing of the Permian mass extinctions; U-Pb dating of closed-system zircons: Science, v. 305, no. 5691, p. 1760-1763.

APPENDIX B. ANALYTICAL METHODS FOR $^{40}Ar/^{39}Ar$ GEOCHRONOLOGY

Berkeley Geochronology Center

Samples analyzed at the Berkeley Geochronology Center were irradiated in the cadmium-lined in-core irradiation tube (CLICIT) facility at the Oregon State University TRIGA research reactor. Samples were irradiated in wells in an Al disk of the type depicted by Renne et al. (1998) along with crystals of Fish Canyon sanidine. J-values were determined as the weighted mean of values (N=8) determined for each of three wells bracketing the samples, and the arithmetic mean and standard deviation (0.0026345 ±0.0000024) of values for these three positions was used for age calculations. Ages are based on the constants of Steiger and Jäger (1977). Age uncertainties do not include contributions from decay constants or age of the standard.

Samples were degassed with a CO_2 laser either by step-wise power increase or by total fusion. Stepwise heating utilized an integrator lens to enhance uniformity of laser power distribution. Analysis with an MAP 215C mass spectrometer followed methods described by Renne et al. (1998). Procedural blanks were measured between every three unknowns and were similar to values reported by Knight et al. (2004). Blank correction was based on regression of data spanning the runs. Mass discrimination (1.00755 ±0.00185 per amu) was determined from analyses of 12 aliquots from an automated on-line air pipette system, regularly interspersed with the unknowns and standards, and the discrimination correction was applied as a power law function (Renne, 2000). Interfering Ar isotopes from Ca, K and Cl were corrected for using production ratios summarized by Renne et al. (2005).

References

Knight K.B., Nomade, S., Renne, P.R., Marzoli, A., Bertrand, H., and Youbi, N., 2004, The Central Atlantic Magmatic Province at the Triassic-Jurassic boundary: Paleomagnetic and $^{40}Ar/^{39}Ar$ evidence from Morocco for brief, episodic volcanism: Earth and Planetary Science Letters v. 228, p. 143-160.

Renne, P.R., Knight, K.B., Nomade, S., Leung, K.-N., and Lou, T.-P., 2005, Application of deuteron-deuteron (D-D) fusion neutrons to $^{40}Ar/^{39}Ar$ geochronology: Applied Radiation and Isotopes, v. 62, p. 25-32.

Renne, P.R., 2000, K-Ar and $^{40}Ar/^{39}Ar$ Dating, in Quaternary Geochronology: Methods and Applications (J.S. Noller, J.M. Sowers, and W.R. Lettis, Eds.): American Geophysical Union Reference Shelf Series, v. 4, p. 77-100.

Renne, P.R., Swisher, C.C., Deino, A.L., Karner, D.B., Owens, T., and DePaolo, D.J., 1998, Intercalibration of Standards, Absolute Ages and Uncertainties in $^{40}Ar/^{39}Ar$ Dating: Chemical Geology (Isotope Geoscience Section), v. 145, p. 117-152.

Steiger, R. H., and Jäger, E., 1977, Subcommission on geochronology: Convention on the use of decay constants in geo- and cosmochronology: Earth and Planetary Science Letters, v. 36, p. 359-362.

University of Nevada, Las Vegas

Samples analyzed by the $^{40}Ar/^{39}Ar$ method at the University of Nevada Las Vegas were wrapped in Al foil and stacked in 6 mm inside diameter Pyrex tubes. Individual packets averaged 3 mm thick and neutron fluence monitors (FC-2, Fish Canyon Tuff sanidine) were placed every 5-10 mm along the tube. Synthetic K-glass and optical grade CaF_2 were included in the irradiation packages to monitor neutron induced argon interferences from K and Ca. Loaded tubes were packed in an Al container for irradiation. Samples irradiated at the Nuclear Science Center at Texas A&M University were in-core for 14 hours in the D3 position on the core edge (fuel rods on three sides, moderator on the fourth side) of the 1MW TRIGA type reactor. Irradiations are performed in a dry tube device, shielded against thermal neutrons by a 5 mm thick jacket of B_4C powder, which rotates about its axis at a rate of 0.7 revolutions per minute to mitigate horizontal flux gradients. Correction factors for interfering neutron reactions on K and Ca were determined by repeated analysis of K-glass and CaF_2 fragments. Measured $(^{40}Ar/^{39}Ar)_K$ values were 0.0002 (± 150%). Ca correction factors were $(^{36}Ar/^{37}Ar)Ca$ = 3.134 (± 7.09%) x 10^{-4} and $(^{39}Ar/^{37}Ar)Ca$ = 7.357 (± 9.92%) x 10^{-4}. J factors were determined by fusion of 4-5 individual crystals of neutron fluence monitors which gave reproducibility's of 0.15% to 0.44% at each standard position. Variation in neutron flux along the 100 mm length of the irradiation tubes was <4%. An error in J of 0.1458% was used in age calculations. No significant neutron flux gradients were present within individual packets of crystals as indicated by the excellent reproducibility of the single crystal flux monitor fusions.

Irradiated crystals together with CaF_2 and K-glass fragments were placed in a Cu sample tray in a high vacuum extraction line and were fused using a 20 W CO_2 laser. Sample viewing during laser fusion was by a video camera system and positioning was via a motorized sample stage. Samples analyzed by the furnace step heating method utilized a double vacuum resistance furnace similar to the Staudacher et al. (1978) design. Reactive gases were removed by a single MAP and two GP-50 SAES getters prior to being admitted to a MAP 215-50 mass spectrometer by expansion. The relative volumes of the extraction line and mass spectrometer allow 80% of the gas to be admitted to the mass spectrometer for laser fusion analyses and 76% for furnace heating analyses. Peak intensities were measured using a Balzers electron multiplier by peak hopping through 7 cycles; initial peak heights were determined by linear regression to the time of gas admission. Mass spectrometer discrimination and sensitivity was monitored by repeated analysis of atmospheric argon aliquots from an on-line pipette system. Measured $^{40}Ar/^{36}Ar$ ratios were 284.31 ± 0.23% during this work, thus a discrimination correction of 1.03938 (4 AMU) was applied to measured isotope ratios. The sensitivity of the mass spectrometer was ~6 x 10^{-17} mol mV^{-1} with the multiplier operated at a gain of 52 over the Faraday. Line blanks averaged 2.04 mV for mass 40 and 0.002 mV for mass 36 for laser fusion analyses and 33.36 mV for mass 40 and 0.08 mV for mass 36 for furnace heating analyses. Discrimination, sensitivity, and blanks were relatively constant over the period of data collection. Computer automated operation of the sample stage, laser, extraction line and mass spectrometer as well as final data reduction and age calculations were done using LabSPEC software written by B. Idleman (Lehigh University). An age of 28.02 Ma was used for the Fish Canyon Tuff sanidine flux monitor in calculating ages for samples.

For $^{40}Ar/^{39}Ar$ analyses a plateau segment consists of 3 or more contiguous gas fractions having analytically indistinguishable ages (i.e. all plateau steps overlap in age at $\pm 2\sigma$ analytical error) and comprising a significant portion of the total gas released (typically >50%). Total gas (integrated) ages are calculated by weighting by the amount of ^{39}Ar released, whereas plateau ages are weighted by the inverse of the variance. For each sample inverse isochron diagrams are examined to check for the effects of excess argon. Reliable isochrons are based on the MSWD criteria of Wendt and Carl (1991) and, as for plateaus, must comprise contiguous steps and a significant fraction of the total gas released. All analytical data are reported at the confidence level of 1σ (standard deviation).

Staudacher, T.H., Jessberger, E.K., Dorflinger, D., and Kiko, J., A refined ultrahigh-vacuum furnace for rare gas analysis, J. Phys. E: Sci. Instrum., 11, 781-784, 1978.
Wendt, I., and Carl, C., 1991, The statistical distribution of the mean squared weighted deviation, Chemical Geology, v. 86, p. 275-285.

APPENDIX C. ANALYTICAL METHODS FOR (U-Th)/He THERMOCHRONOLOGY

Apatites and zircon grains were separated from bulk rock samples by standard crushing, heavy liquid, and magnetic separation techniques and were subsequently handpicked using a binocular microscope. Apatite crystals were selected based on morphology, clarity, and lack of inclusions using a binocular microscope with crossed polars. Zircon selection was based on clarity and crystal morphology. Prior to analysis, grains were photographed and dimensions were measured. Grains were packaged in Pt packets and heated to 1065° C for eight minutes. Extracted He gas was spiked with ^{3}He, purified using cryogenic and gettering methods, and analyzed on a quadrupole mass spectrometer.

Degassed apatites were retrieved, spiked with a ^{235}U-^{230}Th-^{51}V tracer, dissolved in HNO_3 at ~90 °C for 1 hour, and analyzed on a Finnigan Element ICP-MS. Degassed zircons were retrieved, placed in a larger Pt packet with a flux of Li metaborate, heated in a muffle furnace to 1000° C for two hours, and allowed to cool. The resultant bead was spiked with a ^{235}U-^{230}Th-^{51}V tracer, dissolved in HNO_3 and analyzed on a Finnigan Element ICP-MS. A hexagonal prism morphology was used to make an alpha-ejection corrections for each crystal to account for He ejected from crystal margins (Farley et al., 1996). Fragments of the Durango apatite standard were analyzed by the same procedures with the batch of unknowns.

Farley, K.A., Wolf, R.A., and Silver, L.T., 1996, The effects of long alpha-stopping distances on (U-Th)/He ages: Geochimica et Cosmochimica Acta, v. 60, p. 4223-4229.